Eindhoven University of Technology

MASTER

Hydrogen plasma-assisted spatial atomic layer deposition of SnOx

van der Velde, A.

Award date:
2019

Link to publication

ANDY VAN DER VELDE

Hydrogen Plasma-Assisted Spatial Atomic Layer Deposition of SnOx

DECEMBER 2019

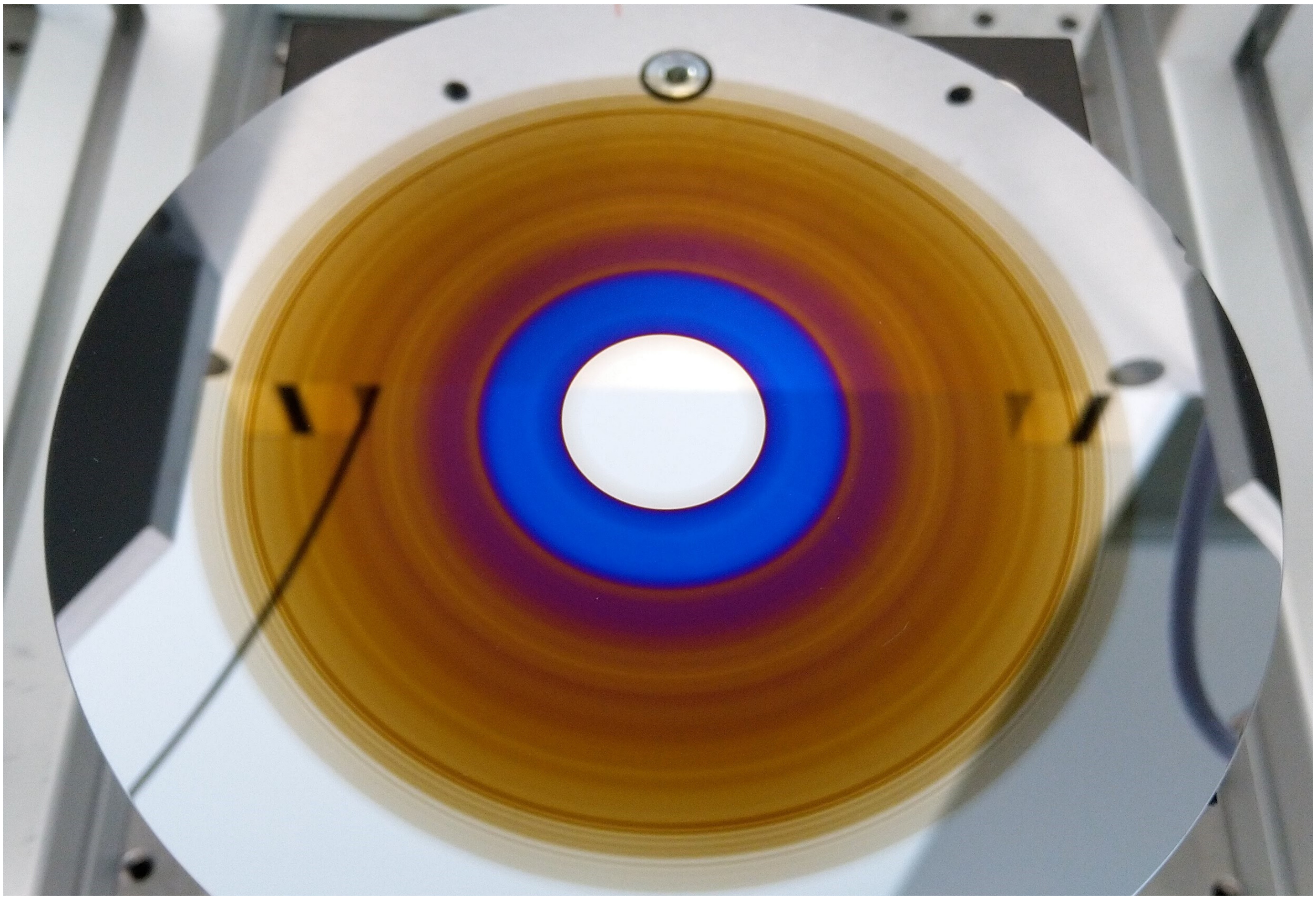

SUPERVISORS

Dhr. C.H. Frijters MSc.
Holst Centre / TNO

Prof.dr.ir. W.M.M. Kessels
Eindhoven University of Technology

Abstract

The fabrication of p-type metal oxide semiconductors on an industrial scale would open up a lot of possibilities for electronic devices. The growth of tin oxide thin films by Spatial Atomic Layer Deposition is investigated with the goal of producing p-type metal oxide thin films on a commercially viable scale. Tetrakis(dimethylamino)tin(IV) is used as a precursor for this process, since it is the only wide-scale available tin precursor for Atomic Layer Deposition. As a tin(IV) precursor, the thermal process with water as a co-reactant results typically n-type tin dioxide thin films however.

Following up on previous research, an in-situ hydrogen-nitrogen plasma is added as an additional step to the deposition process to in-situ reduce the tin to lower oxidation states. Central to this report are the following topics: (i) the feasibility of using this plasma in tin oxide Spatial Atomic Layer Deposition, (ii) the difference in material properties resulting from the thermal and the hydrogen plasma-assisted tin oxide process, (iii) the resulting change reaction mechanisms and (iv) a comparison of these samples to p-type tin monoxide.

A large number of both thermal and hydrogen plasma-assisted tin oxide are deposited and characterized. The effects of exposure time, plasma composition and various other deposition parameters are studied in order to characterize the differences between both processes. The growth per cycle as a function of the exposure time is modelled to investigate possible reaction mechanisms. To determine whether the fabrication of p-type tin oxide thin films is possible a tin monoxide reference sample is obtained for comparison of the material properties.

The growth of hydrogen plasma-assisted tin oxide was shown to be a reproducible process. This process does not result in p-type tin monoxide and is instead similar to the tin dioxide from the thermal deposition process. There are however slight changes in the optical and electrical properties and the hydrogen plasma-assisted samples contain some nitrogen impurities. The most significant difference between the processes is the thermal process having a large deposition temperature dependency, which is not present for the hydrogen plasma-assisted process.

It is concluded that these changes are due to the hydrogen plasma successfully reducing the tin to lower oxidation states, but the tin is re-oxidized when reacting to the water precursor. The growth rate of the hydrogen plasma-assisted tin oxide process is in contrast to the thermal tin oxide not dependent on the amount of hydroxide ligands which form during the deposition. From comparison to kinetic models the growth rate of hydrogen plasma-assisted tin oxide appears to be limited by the amount of precursor dosed to the substrate rather than the chemical reaction rates.

Table of Contents

Abstract **ii**

Table of Contents **iii**

Nomenclature **iv**

1 Introduction **1**

1.1 P-type Metal-Oxide-Semiconductors 2

1.2 Atomic Layer Deposition 2

1.3 Spatial Atomic Layer Deposition 3

1.4 Project Goals and Thesis Outline 5

2 SnOx Thin Films by SALD **7**

2.1 Tetrakis(dimethylamino)tin(IV) precursor 7

2.2 Hydrogen Plasma 8

2.3 Growth Reaction Mechanisms 10

3 Experimental Setup **13**

3.1 SALD Setup Characteristics and Settings 13

3.2 Characterization Techniques 15

3.2.1 Spectroscopic Ellipsometry 15

3.2.2 UV-VIS Spectroscopy 16

3.2.3 Hall Measurements 17

3.2.4 X-ray Photoelectron Spectroscopy 17

3.2.5 X-ray Diffraction 18

3.2.6 Raman Spectroscopy 18

4 SALD Process Development and Evaluation 19

4.1 Plasma-assisted Growth of SnOx 19

4.1.1 Thermal SnOx Growth 19

4.1.2 Plasma-assisted SnOx Growth 20

4.2 Process Evaluation 24

4.2.1 Precursor Order 24

4.2.2 Reproducibility 25

4.2.3 Growth Rate 26

4.2.4 Precursor Dependency 30

4.2.5 Co-reactant Dependency 32

4.2.6 Plasma Composition 32

4.2.7 Deposition Temperature 34

4.2.8 Depositions Without Water 35

4.3 Sample Characterization 37

4.3.1 Electrical Properties 37

4.3.2 Tin Monoxide 38

4.3.3 Material Composition 38

4.3.4 Optical Properties 42

4.3.5 Annealing 44

5 Conclusions and Final Remarks 47

5.1 Conclusions 47

5.2 Outlook 49

Acknowledgements 50

Appendix 51

A Spectroscopic Ellipsometry Models 51

Bibliography 54

Nomenclature

ALD	Atomic Layer Deposition
CVD	chemical vapour deposition
GPC	growth per cycle
IGZO	indium gallium zinc oxide
PVD	physical vapour deposition
SALD	Spatial Atomic Layer Deposition
SDBD	surface dielectric barrier discharge
SE	spectroscopic ellipsometry
SPD	specific precursor dosage
TDMASn	tetrakis(dimethylamino)tin(IV)
TFTs	thin film transistors
XPS	x-ray photoelectron spectroscopy
XRD	x-ray diffraction

Chapter 1

Introduction

In today's society the use of electronic devices is embedded everywhere in our day-to-day lives. A lot of these devices are using silicon-based transistors. In recent years there has been a growing interest in metal-oxide semiconductor materials as the replacement active material in transistors. Metal-oxide semiconductor materials have an excellent charge carrier mobility in the amorphous phase and an high optical transparency[1], which for example allows higher refresh rates for displays and transparent, flexible devices[2,3].

Metal-oxide semiconductor materials can be divided in n-type and p-type materials. N-type semiconductors have free electrons as the majority charge carriers and the Fermi level lies closer to the conduction band. In p-type semiconductors free electrons are the minority carrier and holes are the majority carriers. The Fermi level for p-type materials is below the intrinsic Fermi level and closer to the valence band. Research has mostly been focussed on producing n-type metal-oxide semiconductor materials due to the inherent difficulties of producing p-type materials. N-type materials such as indium gallium zinc oxide (IGZO) are already commercially available as the thin film transistors (TFTs) active material in OLEDs, but p-type materials are as of now unavailable at larger scales.

The importance of developing a suitable p-type MOS is that it creates the possibility of producing complementary metal-oxide semiconductor logic circuit designs such as inventors which utilize both n-type and p-type materials. The fabrication of these logic circuits would result in higher versatility and improvements such as lower power consumption and flexible circuitry.

Within Holst Centre/TNO investigatory studies have been performed[4,5] as part of a larger project to explore the possibility of developing a p-type metal-oxide semiconductors for use in TFTs on a commercially viable scale by using Spatial Atomic Layer Deposition (SALD). Promising results were obtained by using tetrakis(dimethylamino)tin(IV) (TDMASn) and water together with an hydrogen-nitrogen plasma to deposit SnOx. The material was characterized as possibly p-type or an ambipolar material, with a great growth rate of 0.09 nm per cycle. This research is a continuation of the aforementioned Holst Centre/TNO project, following-up on research performed by other students and aims to provide a definitive conclusion about the viability of the above method.

This introduction chapter provides background information about the p-type metal-oxide semiconductor material selection within this project. Afterwards the basics of Atomic Layer Deposition (ALD) will be introduced together with its industrial-scale viable variant SALD. Finally an overview of the project goals and outline of this thesis will be presented.

1.1 P-type Metal-Oxide-Semiconductors

P-type semiconductors are characterized by the usage of holes as the majority charge carriers instead of electrons. This results in an high formation energy for native acceptors as they have to create vacancies and a low formation energy for native donors which easily fill the open vacancies[6]. In this research, p-type metal oxide thin films are of special interest.

An intrinsic problem hinders the development of p-type metal oxides. P-type conductivity is possible due to presence of overlapping oxygen 2p orbitals. The valence band maximum of these orbitals is an anisotropic, which reduces the overlap of the orbitals. This results in an intrinsically low electrical conductivity and low hole mobility[7]. Hybridizing the oxygen 2p orbitals with appropriate orbitals of neighbouring metal cations improves the p-type conductivity as the overlap of the orbitals increases[8].

From the limited number of suitable candidate p-type materials, a couple (Ag_2O, Cr_2O_3, and Co_3O_4) were not considered due to a lack of recent progress and the nature of the project[4]. A material which is intensively researched is NiO, however its toxicity and the extensive risks involved with it ruled it out for further consideration. This resulted in two serious candidates, Cu_2O and SnO.

Of the two materials, Cu_2O has a lower reported bandgap of 1.9-2.0 eV compared to 2.5-2.8 eV for SnO. The Hall mobility of Cu_2O is unmatched however, with values up to 256 $cm^2\ V^{-1}s^{-1}$ reported in literature[9], whereas values for SnO are generally lower than 10$cm^2\ V^{-1}s^{-1}$. The Cu(I) in the material might convert to Cu(II) at room temperature however, which leads to stability issues. SnO also has stability issues, but to a lesser degree. It has a low formation energy and the Sn^{2+} oxidizes to Sn^{4+} at temperatures above 300 °C.

Cu_2O is considered better material due to the significantly higher potential mobility. At the start of the research project within Holst Centre/TNO the Cu_2O precursors were not available, therefore as the second option SnO was investigated instead. This lead to some interesting SnOx thin film layers which sparked further interest, so it was decided to focus solely on SnOx.

1.2 Atomic Layer Deposition

There are numerous methods for thin film fabrication, but generally they can be classified into two categories. The first is physical vapour deposition (PVD) which includes depositions by sputtering, evaporation or sublimation, whereas chemical vapour deposition (CVD) involves depositions form the vapour phase through chemical reactions[10]. Techniques vary on more specific aspects and the processes can be either thermal or plasma enhanced at different pressure ranges.

Atomic layer deposition is a variant of CVD and can be used for low-temperature fabrication of uniform layers with atomic-level thickness control. The key to a successful ALD deposition process is to devise a reaction scheme consisting of a sequence of discrete, self-limiting adsorption and reaction steps[10]. Conventional ALD is therefore typically based on a four-step process. The precursor is pulsed into the deposition chamber and reacts with the surface until all surface sites are consumed, after which a purging step takes place with a non-reactive gas such as nitrogen to remove all residual reactant. The third step in the process is the injection of a co-reactant, which reacts to the precursor surface ligands. This is followed by another purge. The result is a self-limiting reaction, as the precursor can only react to surface sites where the co-reactant is located and vice-versa. Any additional growth due to physisorption is removed by the non-reactive purge gas, resulting in monolayer-by-monolayer growth of high-quality thin films.

To obtain a certain desired thickness, the four-step process just needs to be repeated, as the thickness is only dependent on the number of cycles.

1.3 Spatial Atomic Layer Deposition

The major drawback of ALD is its low deposition rate, which makes the technique unsuitable for the intended industrial-scale applications of the Holst Centre/TNO project. An alternative approach to this technique is Spatial Atomic Layer Deposition (SALD), where the half reactions are separated spatially instead of through the use of purge steps in time[11]. This concept is illustrated in Figure 1.1. The main advantage of the SALD approach is that the purge times are significantly reduced. Therefore, the completion time of a single ALD cycle is no longer limited by the individual step times, which are in the order of seconds. Instead it is limited by the kinetics of the specific reactions involved. Due to a continues supply of precursor, this is in the order of tens of milliseconds instead.

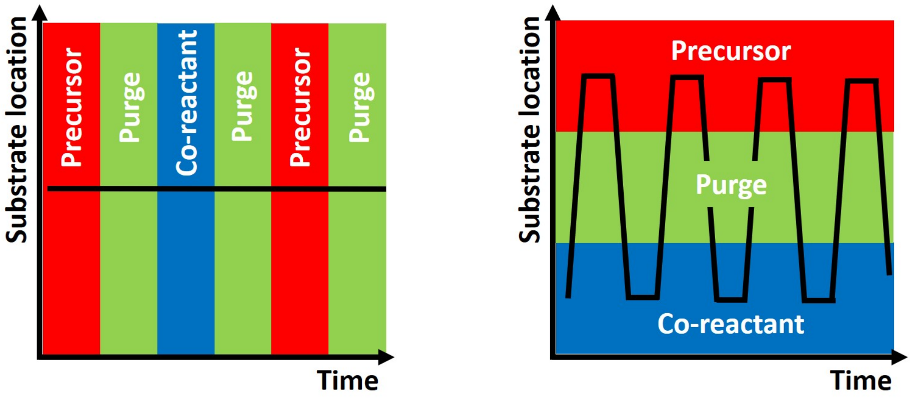

(a) ALD **(b)** SALD

Figure 1.1: The conceptual difference between ALD and SALD schematically visualized. For ALD the substrate is stationary and the environment is changed over time, during SALD the environment is fixed and the sample changes in location, reducing the time per cycle significantly as the purge steps between dosages become obsolete. Based on Poodt et al.[11].

The main challenge in ALD is the prevention of precursor intermixing. The purge steps between the half reactions remove surplus precursor form the reaction chamber, so no mixing takes place. During SALD the precursors are separated in location instead, and the sample travels between both zones. The purging in SALD happens through the use of an inert gas zone such as nitrogen in between the precursor zones.

Successful SALD concepts are for example roll-to-roll, sheet-to-sheet and rotational SALD, of which the latter will be used in this research. In rotational SALD, a gas injector head with different precursor slots remains stationary, while a sample substrate rotates underneath. This is schematically shown in Figure 1.2. On the left side the reactor head is shown. The precursor gasses enter from the inlets at the bottom and exit at the different precursor outlets shown as blue and green. In purple a plasma-slot is shown, which is further discussed in section 2.2. Shown as small orange dots are the outlets for the inert gas curtains which are used for purging.

The reactor head is situated in an oven, which is set to the desired deposition temperature, with the reactive gasses and exhaust coming in from the top. It is supported by a gas bearing, and when properly designed, the pressure field resulting from the gas flow out of the inert gas curtains can support the reactor

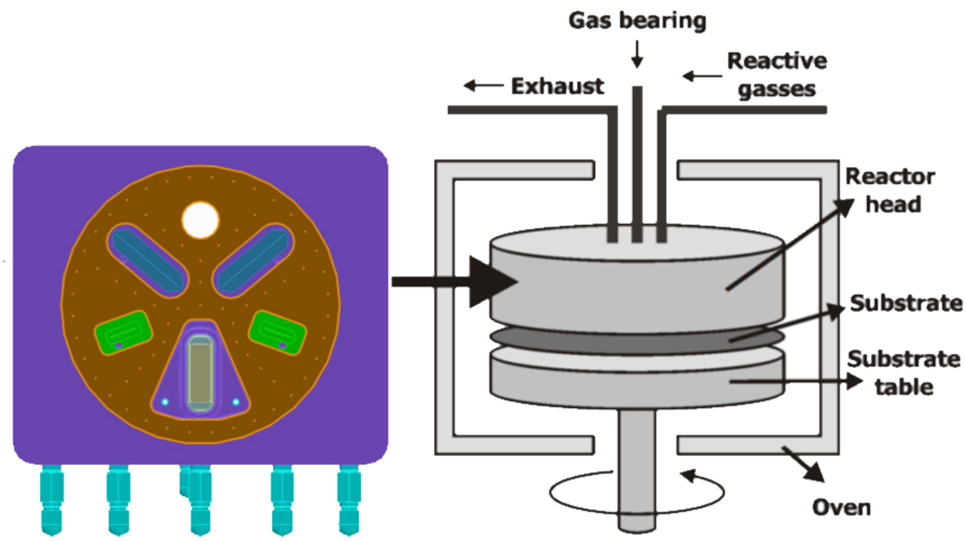

Figure 1.2: An overview of the rotational SALD concept. On the left the bottom of the reactor head is shown from below with the precursor slots (small green, large blue), plasma slot (purple) and nitrogen curtain outlets (organge dots) visible. The right side of the image shows schematically the incorporation of the reactor head with the other parts. Courtesy of Poodt et al.[12].

head just micrometers above the substrate[13]. This removes the the need for high-tolerance mechanical fixtures. The substrate is placed on a rotatable substrate table, which is powered by a motor from the bottom.

As mentioned before in this section, the cycle time of SALD is limited by the kinetics of the reaction taking place. In contrast to conventional ALD, where the optimal time step for each step in a cycle can be determined individually, for rotational SALD all step times are equal as the sample rotates with a constant velocity. It is necessary to adjust this velocity to the reaction step which has the slowest reaction kinetics in order to reach saturated growth. This reaction is called the rate-limiting reaction and differs for each process. The exposure time t can by calculated by

$$t = \frac{W}{2\pi r \nu} \tag{1.1}$$

where W is the width of the precursor inlet, r the radial position on the substrate and ν the rotation frequency. The exposure time being dependent on the radius results in a range of exposures being measurable on the same sample. On these samples large variations in material properties can therefore be seen, especially in the close-but-not-yet-saturated region. This variation is unfavourable for industrial applications as a uniform layer is preferred, but can be considered an advantage for usage as a research tool. For studies on the exposure time dependency of the reaction a range of exposure times can be measured with a single sample. For optimized tools dedicated to producing a single material, it is possible to optimize the precursor slot widths and shape. For instance, a pie-shaped precursor slot could compensate for this radial dependency.

For SALD processes, the growth per cycle (GPC) is a function of the precursor partial pressure and the exposure time on the surface. When the partial pressure is too low or the exposure time is too short, the ALD growth will be unsaturated, since not all available surface ligand groups react to the precursor molecule. If increasing the exposure time of the reaction does not lead to an increase in the amount of precursor that is absorbed onto the surface, the surface is considered saturated and the GPC will not further increase. Note that possible factors such as steric hindrance also prohibit the precursor molecule from reacting with the surface ligands, which limits the possible growth. Undersaturated film growth results in less material being added to the thin film each ALD cycle, so the GPC decreases. Fitting the GPC against the exposure time with various models might therefore yield information about the processes which play a role in the thin film growth.

1.4 Project Goals and Thesis Outline

The focus of this research is the realization and the advanced exploration of the hydrogen plasma-assisted SnOx Spatial Atomic Layer Deposition process for the production of p-type metal oxide semiconductor thin films. Within Holst Centre/TNO previous research was conducted by two other students on this topic, which focussed on identifying a possible SALD process for p-type thin films[4] and the production of p-type TFTs[5] from the thin films found in the former research. Using this research as a basis, the following project goals can be defined.

- Investigate the feasibility of using hydrogen plasma as an additional step to the thermal SnOx process.
- Analyse the reaction mechanisms and evaluate the effects of various growth parameters.
- Describe the difference in materials produced by the thermal and plasma-assisted SnOx process, and compare those to tin monoxide.

In the earlier stages of this research an additional goal was the production of functional TFTs. However, dissatisfactory results made it clear that the quality of the material was not fit for this. Therefore, the decision was made to drop this goal from the project and put more focus on the underlying mechanics.

For the outline of this thesis, this past chapter gave the motivation for this research and background information on p-type metal-oxide semiconductor, ALD and SALD as an introduction to this research. The second chapter will focus more in-depth on the plasma-assisted deposition of SnOx thin films by considering precursors, the effect of in-situ hydrogen plasma on the growth and give an overview of the current state-of-the-art on this subject.

Following this the experimental set-up will be discussed in Chapter 3, together with the various characterisation methods used in this research. The bulk of this thesis consist of Chapter 4, SALD Process Development and Evaluation, which will give an overview of the results. This chapter is split into three parts, each corresponding to one of the above project goals. The conclusions drawn from these results will be summarized in the final chapter, which also has an outlook with starting points that can serve as the basis for further research.

Chapter 2

SnOx Thin Films by SALD

Where the previous chapter provided the motivation, material choice and global background information on the SALD deposition technique, this chapter aims to focus on the specifics of producing SnOx thin films by SALD. The first part of this chapter covers the different precursor possibilities, such as TDMASn. An innovative solution to reduce the oxidization state was implemented in the form of an hydrogen plasma, which will be discussed in the second part. The final part of this chapter gives the current state-of-the-art of the production of p-type SnOx by SALD using TDMASn.

2.1 Tetrakis(dimethylamino)tin(IV) precursor

Crowell et al.[10] formulated three fundamental properties that a precursor needs to posses in order to be fit for ALD: First it must have enough vapour pressure to be transported to the substrate surface, secondly after a chemical reaction it should easily decompose into desirable reactive species at relatively low temperatures and thirdly it should not react in the gas phase.

Within literature multiple precursors and co-reactants are found which fulfil these requirements and result in SnO2, such as $SnCl_4$[14], $Sn(edpa)_2$ with an O_2-plasma[15] and SnI_4[16]. Precursors which form SnO are rare, but do exist such as an alternative $Sn(edpa)_2$ process[15], $Sn(dmamp)_2$[17] and bis[bis(trimethylsilyl)amino]-tin(II)[18]. However, all of the tin monoxide precursors and quite a lot of the tin dioxide precursors are not commercially available. This makes them unsuitable to use in industrial applications for the large-scale production of p-type TFTs.

There is a tin oxide precursor available which is commercially available in larger quantities, TDMASn. Elam et al.[19] were the first to show SnO_2 grown from TDMASn with H_2O_2, H_2O and O_3 as co-reactants. Since then, TDMASn with either H_2O_2[20,21], O_3[21,22,23,24] or H_2O[21,22] is extensively used in research. In other works O_2 plasma is also used as a possible co-reactant[25,22].

Of these possible co-reactants, H_2O behaves different from the rest. The resulting thin film layer are grown with a lower GPC and posses a higher refractive index and lower bandgap[21,26] compared to the other precursors. Both effects are a possible indication of an higher amount of tin monoxide in the layer. Therefore, as this research aims to produce p-type thin film layers, water is chosen as the co-reactant.

The deposition reaction of TDMASn (chemically $Sn(DMA)_4$)and H_2O is as proposed by Mullings et al.[21]

$$\mathrm{OH}_x^* + \mathrm{Sn(DMA)}_4 \rightarrow \mathrm{(O)}_x\text{–}\mathrm{Sn(DMA)}_{4-x}^* + x\mathrm{HDMA} \uparrow . \tag{2.1}$$

The surface group is indicated with $*$, and $\uparrow$ is used to indicate groups leaving the reaction site as a gas. As TDMASn can release up to four ligands, x is used the average amount of released ligands. The water half-reaction has a similar form as seen below.

$$\mathrm{(O)}_x\text{–}\mathrm{Sn(DMA)}^*_{4-x} + 2\mathrm{H_2O} \rightarrow \mathrm{SnO_2}\text{–}\mathrm{(OH)}^*_x + (4-x)\mathrm{HDMA}\uparrow \tag{2.2}$$

The reaction rate of this water half-reaction has a dependency on the chemical environment. Tanskanen et al.[27] have shown neighbouring hydroxide groups on the surface facilitate the water half-reaction, increasing the reaction rate of this process.

When water as a co-reactant is compared to H_2O_2, the growth rate of the reaction with water is lower due to steric hindrance. The DMA groups on the surface prevent a large part of the water molecules to react with the surface. The result is the average amount of released ligands x is 2.5 for H_2O and 3.2 for H_2O_2[19]. This corresponds to respectively 37% and 20% of the ligands remaining on the surface.

Although TDMASn is well-researched, readily commercially available and produces high-quality thin films, the process results in n-type tin dioxide. This research focusses on the possible production of p-type monoxide, and the main challenge is finding a method which results in an oxygen-deficient layer. The average oxidization of the tin atoms in the thin film layer needs therefore to be reduced from Sn^{4+} to Sn^{2+}. A possible mechanism for reducing metal-oxides is the application of an hydrogen plasma. Investigating the viability of the in-situ usage of an hydrogen plasma for the production of p-type SnOx is the main focus of this research.

2.2 Hydrogen Plasma

Hydrogen Reduction of Tin Oxide

In 1984, Schade et al.[28] reported on the interactions of hydrogen plasma with tin oxide layers. They found that the positive hydrogen ions in the plasma lead to a chemical reduction of the tin oxide surface, resulting in decreased optical transmission by formation of an absorbing oxygen-depleted surface layer. The XPS data showed a shift of the Sn^{4+} peak towards lower binding energies, at which Sn^{2+} and Sn^0 can be found, so their conclusion was that the surface layer contained some tin monoxide and metallic tin.

In recent years this effect is better understood and shown for a large variety of metal oxides. The chemical reaction due to the hydrogen plasma for tin dioxide can be represented as[29]

$$\mathrm{SnO_2} + x[\mathrm{2H/2H^+/2H^{2+}/2H^{3+}/H_2^*}](\mathrm{p}) = \mathrm{SnO}_{2-x} + x\mathrm{H_2O(g)} \tag{2.3}$$

with $0 \leq x \leq 2$. The reaction is spontaneous, as the Gibbs free energy change is negative[29]. This process has been successfully utilized in-situ in sputtering p-type SnO thin films[30] and in post-deposition processing of SnOx by ALD[24]. In this research the goal is the utilization of hydrogen plasma in-situ for the deposition of tin monoxide thin films by SALD.

Plasma-assisted Atomic Layer Deposition

Plasma-assisted ALD, also called plasma-enhanced ALD, is the term coined for the usage of plasmas within ALD processes. Utilizing plasmas in ALD has for instance lead to breakthroughs in high-volume manufacturing, an increased amount of materials that can be processed by ALD, low temperature depositions and area-selective ALD[31]. The driving force behind plasma ALD is the significantly increased reactivity of reactant species in a plasma environment compared to standard thermal ALD.

Within standard plasma-assisted ALD the co-reactant is a plasma. However, in this research a hydrogen/nitrogen step will be added to the ALD cycle while keeping water vapour as the main co-reactant. A mixture of hydrogen and nitrogen instead of pure hydrogen in the plasma is necessary for safety reasons. Nevertheless, plasma-assisted ALD will in this report be used as an umbrella-term encompassing all ALD processes which utilize any form of plasma. The term thermal SnOx will henceforth be used to describe the two-step [TDMASn, H_2O] deposition process, while plasma-assisted SnOx will refer to the three-step [TDMASn, H_2O, H_2/N_2 plasma] deposition process.

The plasma used in this research is an atmospheric surface dielectric barrier discharge (SDBD) remote plasma. Operating under atmospheric pressure, the plasma source as seen in Figure 2.1 generates a plasma 200 µm above the substrate surface. The geometry of the plasma source allows the generation of a SDBD plasma in close vicinity of the substrate without charging the thin film or the substrate[32], which might lead to inhomogeneous depositions. The gas velocities reach high velocities up to 10 m/s, so the reactive species can reach the substrate surface.

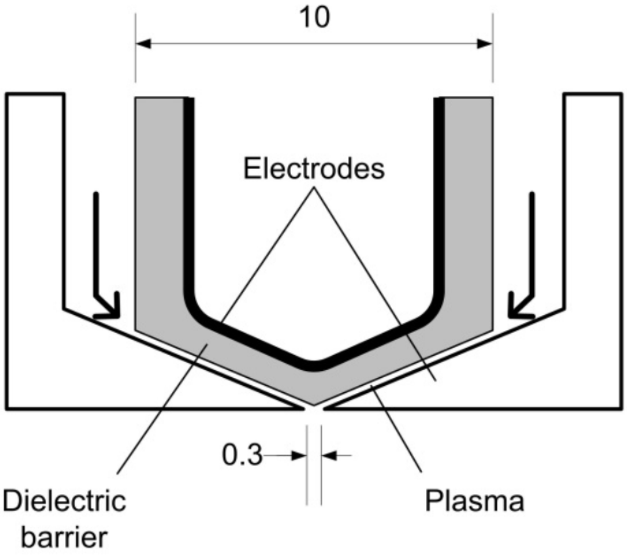

Figure 2.1: A schematic overview of the indirect plasma source. The gas enters from the top, follows the arrows and is converted to a plasma before exiting out the bottom. The dimensions are in millimetres. Courtesy of Creyghton et al.[32]

Hydrogen and Nitrogen Doping

The application of an hydrogen plasma can result in hydrogen doping of the tin oxide. Hydrogen is known to be amphoteric in semiconductors, meaning that it counteracts the dominant conductivity of the material[33]. Thus in n-type semiconductors hydrogen can cancel out the dopants inducing electrically active states in the form of shallow acceptor levels. The effect on n-type tin oxide would be the material becoming ambipolar, possessing both n-type and p-type properties[34].

The application of an hydrogen/nitrogen plasma could not only result in doping, but may even cause the growth of metal nitrides. The growth of for example TaN_x by ALD has been shown by using an hydrogen/nitrogen plasma as a co-reactant[35]. Steward et al.[36] used a nitrogen plasma to create tin oxynitride by ALD, also using TDMASn and H_2O as precursors. By controlling the dose ratio of water and hydrogen, they were able to change the nitrogen:oxygen ratio of the material between 0 and 0.95. As nitrogen is used as a carrier gas for the hydrogen in this research, there is a possibility for the creation of tin oxynitride with the plasma-assisted SnOx process. To prevent this a noble gas as argon of helium could be used, but this is not possible with the current set-up.

The nitrogen plasma needs very long exposure times (>20 seconds) however to remove the methyl ligands and saturate the surface[36]. The SALD process used in this research uses exposure times from 20ms to 400ms, a factor of 50-1000 times lower. This time scale difference is considered significant enough for this effect not to take place. Nitrogen incorporation in the material is therefore still a possible side-effect of this process, but the expected values are expected to be negligible.

2.3 Growth Reaction Mechanisms

Growth as a function of exposure time

In this research the growth rate of the reaction, the growth per cycle as a function of the exposure time will be investigated in order to study the effects of the hydrogen/nitrogen plasma. The addition of plasma is expected to cause different chemical reactions to take place compared to the thermal ALD reaction, so the growth rate will differ accordingly. Following Poodt et al.[12], a basic model which gives the GPC as a function of the exposure time will be derived which is based on the Langmuir isotherm.

Under fixed temperature, precursor partial pressures and exposure time for the duration of the deposition, the GPC can be expressed as a function of the net surface coverage of the precursors. In the ALD process, one of the reaction is expected to take place at longer timescales than the other reactions. This is called the rate-limiting reaction and can be caused by a limited supply of precursor or the nature of the reaction kinetics. Either way, the corresponding surface coverage of the reaction products after the rate-limiting reaction is the rate-limited surface coverage θ. The surface coverage can be expressed as a function of the exposure time $\theta(t)$, as the surface coverage will always go to 1 for long exposure times and 0 for very short exposure times. This can be used for the exposure time dependent $GPC(t)$ as

$$GPC(t) \approx GPC_{sat}\theta(t) \tag{2.4}$$

with GPC_{sat} the GPC at long exposure times and full surface coverage.

Following the Langmuir isotherm, the change in precursor surface coverage as a function of the exposure time is equal to the adsorption rate r_{ad} minus the desorption rate r_d. Both can be expressed as a function of the surface coverage, as r_{ad} scales with the adsorption reaction rate k_{ad} [Pa^{-1}], the precursor gas concentration on the substrate in the form of the precursor partial pressure p [Pa] and the unoccupied part of the surface $1 - \theta$. The dimensionless desorption reaction rate k_d scales only with surface coverage, resulting in

$$\frac{d\theta(t)}{dt} = r_{ad} - r_d = k_{ad} \cdot p \cdot (1 - \theta(t)) - k_d\theta(t). \tag{2.5}$$

This differential equation can be solved to obtain

$$\theta(t) = \frac{k_{ad} \cdot p}{k_{ad} \cdot p + k_d} \cdot (1 - \exp(-(k_{ad} \cdot p + k_d)t). \tag{2.6}$$

Recalling Equation 2.4 and assuming a constant partial pressure and reaction rate, the GPC as a function of the exposure time can be written as

$$GPC(t) = GPC_{sat} \cdot (1 - \exp(-at)) \tag{2.7}$$

with GPC_{sat} the GPC at exposure times for which the reaction is saturated in which the constant first part of Equation 2.6 is incorporated and a a fitting constant for the time dependency of the exponential function.

When plotting the GPC versus the exposure time, the basic model in 2.7 can be applied to obtain an estimate for the saturation GPC and the reaction rate. This will be applied to the data in section 4.2.3. However, as this model is based on some crude assumptions: (i) a single reaction taking place, (ii) a constant partial pressure and reaction rate, (iii) reaction kinetics limiting the rate instead of for example the supply of precursor and (iv) no CVD growth takes place. Therefore, it is not always applicable to the data. More elaborate models can be tested which do incorporate CVD growth terms, multiple similar rate-limiting reaction rates or different time dependencies. For assumption (iii), an alternative approach is using a model based on the precursor dose instead of the chemical reaction rate, as explained in more detail below.

Growth as a function of dosage

The Langmuir model above is based on the reaction rate k scaling with the partial pressure p, as the latter is proportional to the gas concentration in a system. The partial pressure is assumed to be constant, but in the limit of small partial pressures the equation does not hold as there is too little material supplied to the reaction site. In these cases, the rate-limiting factor is not the time for the chemical reaction to take place, but the precursor supply.

Maydannik et al. proposed an alternative method of determining the molecule concentration for the reaction, by looking at the precursor dosage instead[37]. The precursor concentration at the surface is in this case defined as the number of precursor molecules deposited over an area. Specifically, they coined the specific precursor dosage (SPD) (mol m^{-2}cycle^{-1}), defined as

$$SPD(t) = \frac{N}{A}t \tag{2.8}$$

with N (mol s^{-1}) the total precursor particle influx into the reaction zone, A (m^2) the substrate surface covered by the precursor inlet and t (s cycle^{-1})the exposure time to which the substrate area is subjected to each ALD cycle. If no thermal decomposition or precursor condensation between precursor bubbler and ALD head is presumed, the precursor particle flux N is proportional to the precursor vapour flow rate produced in the bubbler and can be calculated by using the Avogadro constant and the molar volume of gasses under standard conditions.

A model can be derived from here which gives the GPC as a function of the SPD instead of the exposure time. Although also based on Langmuir kinetics like the model in Equation 2.7, it differs in the taken assumptions. Of course this model still contains an dependency on the exposure time, but now the time-dependency is assumed to be the result of the time it takes to apply a certain amount of molecules instead of the time necessary for the chemical reaction to take place. Franke et al.[38] successfully utilized the model which will be derived below.

For this model to work, the surface coverage is defined slightly differently. The GPC is considered to be proportional to the amount of chemisorbed material Q over the maximum possible amount Q_{max} that can be adsorbed on the surface, or

$$\frac{Q}{Q_{max}} = \frac{GPC}{GPC_{sat}}. \tag{2.9}$$

In contrast to the previous model which used the pressure-based Langmuir model, the concentration-based Langmuir model will be used instead. The SPD is used as the local concentration. As this model will be based on the reaction being limited by amount of precursor and therefore assumes the reaction time to be sufficiently large, the time-dependent exponential term in Equation 2.6 will be set to zero as $\exp(-\infty) \rightarrow 0$. With this assumption the Langmuir model from Equation 2.6 can be rewritten as

$$Q(t) = Q_{max}\frac{K \cdot SPD(t)}{1 + K \cdot SPD(t)}. \tag{2.10}$$

with $K = \frac{k_{ad}}{k_d}$. Due to its dependency on the deposited area and exposure time, it should be noted that the SPD is a characteristic of particular reactor arrangement and likely to vary with reactor volume and process parameters. Despite this, it predicts the behaviour of an ALD reaction when the process is limited by precursor supply rather than the time it takes for chemical reactions to occur and will be referred to as the dosage-limited model.

As the ALD processes in this research are assumed to not contain any CVD growth, Equations 2.9 and 2.10 can be rewritten to calculate the GPC as

$$GPC(t) = GPC_{sat} \cdot \frac{K \cdot SPD(t)}{1 + K \cdot SPD(t)}. \tag{2.11}$$

Despite this equation being derived from Equation 2.6 just like Equation 2.7, both model predict a different GPC versus exposure time curve. By fitting the models to the data some information about the underlying reaction mechanisms, reaction rate-limited or precursor dosage-limited, can be deduced. This precursor dosage-limited has an additional advantage, as it could also be used for varying the precursor flow into the reactor instead of only an exposure time series.

Hydroxylation

While the chemical reactions shown in Equation 2.1 and 2.2 explain the main ALD reactions, more chemical reactions can occur. Two neighbouring hydroxide ligands can for example combine in a process called dehydroxylation[39]. Water vapour can be released from the sample surface, with an oxygen atom binding to two tin atoms simultaneously as

$$2\text{Sn–OH}^{*} - > \text{Sn–O}^{*}\text{–Sn} + \text{H}_2\text{O(g)}. \tag{2.12}$$

As the TDMASn reacts to hydroxide surface sites, dehydroxylation reduces the number of available surface sites and limits the growth. At higher temperatures at which dehydroxylation increases the GPC is therefore expected to be lower and might becoming a limiting factor to the film growth rate.[39]

The reverse reaction, rehydroxylation, can also occurs in two different versions, depending on whether the resulting hydroxyl groups are bound to the same tin atom. It is given by

$$\text{Sn–O}^{*} + \text{H}_2\text{O(g)} - > \text{Sn–(OH)}_2^{*}. \tag{2.13}$$

Rehydroxylation is, like dehydroxylation, always present but occurs more often for lower temperatures. For adjacent ions to reaction can be given by

$$\text{O–Sn–O}^{*}\text{–Sn} + \text{H}_2\text{O(g)} - > \text{HO}^{*}\text{–Sn–O}^{*}\text{–Sn–OH}^{*}. \tag{2.14}$$

These reactions are effectively oxidizing the tin atoms, changing Sn^{2+} to Sn^{4+}. Where the hydrogen plasma to successfully reduce the Sn^{4+} to lower oxidation states, the application of large amounts of water might undo this process.

Chapter 3

Experimental Setup

3.1 SALD Setup Characteristics and Settings

The SALD reactor used in this research is the rotary POP1 reactor, developed by TNO in 2009. It was used as a proof-of-principle set-up to demonstrate the use of gas bearings for separation of the half-reactions. The core part of the set-up is the reactor head, as shown in Figure 3.1. It consists of two large precursor slots (blue) which are used to dose the TDMASn precursor and water to the substrate, two smaller precursor slots (green) which are unused in this project, an optical hole for in-situ measurements (white) and a plasma slot (grey/purple) which is used to add the hydrogen/nitrogen plasma. The gas bearing outlets are depicted as the small dots (orange), and the gas lines are shown in cyan. The gas bearings outlets are tiny 0.2 mm holes from which nitrogen flows. The nitrogen flow suspends the reactor head 20µm above the substrate. As the flow necessary to perform this suspension is significant, the nitrogen also performs as a reaction zone separator. Precursor gas cannot flow from one side to the other side of these nitrogen curtains due to the backflow of this nitrogen. This effectively separates the different reaction steps spatially.

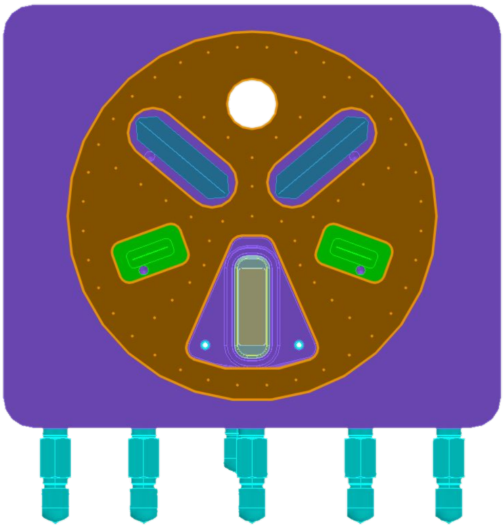

Figure 3.1: An overview of the bottom of the reactor head, which is present in the POP1 rotary SALD setup.

The reactor head is pneumatically extended to the substrate table, providing a downward force to counteract the force from the gas outlets. Changing the downward force varies gap the height. The precursor slots are situated deeper within the head than the gas outlets, so a suspension of 20 µm corresponds with a 120 µm distance between the precursor slot and the substrate. The substrates used in this research are standard 15 cm in diameter Si wafers and 2 mm, 15x15 cm borosilicate glass panes.

The substrate is clamped to the table by a vacuum pump. The substrate table rotates with an adjustable servo motor, enabling for a large range of rotation frequencies. The rotation of the sample under the reactor head results in a 'doughnut-shaped' thin film layer, as shown later in Figure 4.2.

The injector setup is situated in an oven to ensure correct deposition temperatures, for this research between 100 °C and 200 °C. The gasses need to be heated to the same temperatures for the process. However, the gasses are not present in the oven long enough to reach the correct temperatures. Therefore all gaslines are encapsulated with heating wire. For the precursor gasses it also prevents the condensation of the gasses within the lines.

Precursor injection takes place within the small slit in the precursor slots, which are surrounded by exhaust zones to collect the precursor vapour residue and reaction product. These waste products can be toxic, so the exhaust lines flow through a set of scrubbers filled with HCl and water before the waste gasses are sent to the main exhaust. As precursor gasses are spread over the whole slot, the width of 12 mm of the slots will be used to calculate the exposure time of the precursor with Equation 1.1. For the TDMASn and H_2O reaction approximately 800 cycles are needed to obtain 50-60 nm thin films for characterization measurements.

The precursors are liquid at standard conditions and for ALD vapour is necessary. Precursor vapour is extracted by putting the precursors in a bubbler. A bubbler consist of a metal container with two tubes for the inflow and outflow of gasses. The liquid precursor is put at the bottom of this container, leaving enough overhead space so the liquid is not in contact with the inflow or outflow tubes. Due to the vapour pressure of the liquid P_{vapour}, the gas in the overhead compartment will be a mixture of the inflowing argon gas and precursor vapour. As it is an open system, the pressure within the overhead compartment will be equal to the reactor pressure $P0$, which is equal to atmospheric pressure. The gas mixture will therefore flow out the other tube at the same rate as the gas flow into the bubbler,$Q_{bubbler}$. This process delivers precursor vapour to the reactor. The precursor flow $Q_{precursor}$, which is only the amount of delivered precursor in mole s^{-1}, is therefore

$$Q_{precursor} = Q_{bubbler} \frac{P_{vapour}}{P_0 - P_{vapour}}. \tag{3.1}$$

For TDMASn the vapour pressure P_{vapour} is taken as approximately 0.1 Torr[40] at room temperature. The temperature of the water is varied from 5 - 50 °C , and the vapour pressure will be calculated with the Buck equation.

In order to ensure a steady gas flow, an additional argon gas line with flow Q_{dilute} is added as a dilute to the flow from the bubbler to raise the flow rate. Due to the length of the gas lines, a 20 second build-up waiting time is recommended between opening the precursor bubblers and starting the SALD process to ensure the steady-state amount of precursor reaching the reactor. For all ALD processes, an important factor for the reactions is the precursor partial pressure $P_{precursor}$. This can be calculated from the given parameters as

$$P_{precursor} = P_0 \frac{Q_{precursor}}{Q_{bubbler} + Q_{dilute}}. \tag{3.2}$$

Standard depositions in this research have a 500/500 sccm bubbler/dilute argon flow to deliver the precursors to the reactor, but can be varied from 50/950 sccm to 1000/0 sccm.

The plasma slot consist of a SDBD plasma source as shown in Figure 2.1. It has the capability of exerting hydrogen or oxygen plasma, with additional nitrogen to keep the composition well within safety limits. However possible, it is not advisable to simultaneously generate an oxygen and an hydrogen plasma for obvious reasons. This additional plasma slot opens up the possibility to deposit thin film layers with three steps ALD cycles, which will be discussed in section 4.2.1. In order to generate a suitable plasma, voltage and frequency are set to 125V and 50 kHz. For a better overview the settings mentioned in this section are summarized together with the ranges used in this research in the table below.

Table 3.1: An overview of the default settings of the POP1 set-up and the parameter ranges used in this research,

Setting	Default value	Range
Deposition temperature	150 °C	100-200 °C
Number of cycles	800	200-4200
Rotation frequency	60 RPM	10 - 240 RPM
TDMASn bubbler flow/dilute	500/500 sccm	50/950 sccm - 500/500 sccm
TDMASn bubbler temperature	Room temperature	Room temperature
H_2O bubbler flow/dilute	500/500 sccm	50/950 sccm - 1000/0 sccm
H_2O bubbler temperature	35 °C	5 - 50 °C
H_2/N_2 plasma flow	2000/8000 sccm	0/10000 sccm - 2000/8000 sccm
Plasma settings	125V, 50kHz	125V, 50kHz

3.2 Characterization Techniques

3.2.1 Spectroscopic Ellipsometry

In this research the most often used characterisation technique is spectroscopic ellipsometry (SE). SE is a method which utilizes the change in polarized light after reflecting of a materials surface. It allows for a non-destructive method of measuring the thickness and optical properties such as the refractive index of thin films. A schematic overview of this technique is shown in 3.2. Monochrome polarized light is emitted and reflected on the sample under angle θ. Due to reflection the incident light E_i undergoes a phase and amplitude shift, so E_i differs from the reflected light E_r. By varying the energy of the incident light form 1.5 to 5.5 eV a full wavelength spectrum of these shifts is obtained.

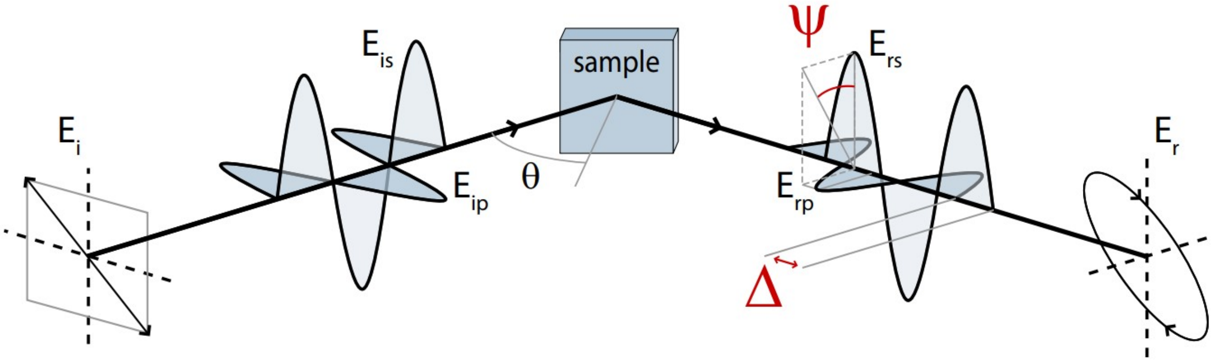

Figure 3.2: A schematic overview of the principles of SE measurements, showing the orientation change of the electromagnetic field E due to refraction under angle θin terms of parameters ψ and Δ. Courtesy of Braecken[41].

The SE detector measures complex ratio ρ of the Fresnel reflection coefficients r_p and r_s, which are respectively the in-plane and perpendicular to the plane of incidence coefficients. This results in two output parameters, the phase difference Δ and amplitude difference ψ in accordance to the relation

$$\tan(\psi)\exp(i\Delta) = \rho = \frac{r_p}{r_s}. \tag{3.3}$$

The material properties cannot be calculated directly from these output parameters, but are instead deduced by fitting different SE models to the data. The choice of model depends on the material properties, film thickness, quality of the data and the preferred type of predicted data. The most significant data types for this research are the film thickness, for the determination of the GPC, and the refractive index. The latter is one of the main indicators of whether the material corresponds to tin monoxide or dioxide. An overview of different relevant SE models can be found in Appendix A.

The output parameters Δ and ψ can be directly related to the complex dielectric constant ε or its real and imaginary parts ε_r and ε_i with[42]

$$\varepsilon = \varepsilon_r + i\varepsilon_i = \sin^2\theta + \sin^2\theta\tan^2\theta\left(\frac{1-\rho}{1+\rho}\right)^2. \tag{3.4}$$

This in turn can be used to obtain the complex refractive index $\tilde{n}$ from ε with

$$\tilde{n} = n + ik = \sqrt{\varepsilon}. \tag{3.5}$$

with n the refractive index and k the extinction coefficient. This also implies $\varepsilon_r = n^2 - k^2$ and $\varepsilon_i = 2nk$. The components ε_r and ε_i are functions of the energy E and are not independent, but obey the Kramer-Kronig relation

$$\varepsilon_r(E) = \varepsilon_r(\infty) + \frac{2}{\pi}\cdot\mathcal{P}\cdot\int_{E_g}^{\infty}\frac{\xi\cdot\varepsilon_i(\xi)}{\xi^2 - E^2}\xi \tag{3.6}$$

where $\mathcal{P}$ is the Cauchy Principle value so the integral can be evaluated. This complex dielectric constant or the complex refractive index can be fitted by the models in Appendix A, so the film thickness and possibly other material properties can be deduced.

In this research a HORIBA UVISEL2 is used in conjecture with DeltaPsi software for ex-situ measurements. Under an angle θ of 70 °, each sample is characterized at multiple position as determined in section 4.1.2. The default refractive index deduced from these results are at a wavelength of 632 nm. A typical result is a thickness of 60 nm and an uncertainty resulting from the model of 1 nm, which typically corresponds to an uncertainty of ± 0.0015 nm/cycle for the GPC. Due to this the error bars are often not significant enough to show in figures resulting from SE measurements. In this error a couple of factors like measurement uncertainty, inhomogeneity of the samples and such are neglected.

3.2.2 UV-VIS Spectroscopy

The transmission, reflection and other derived optical properties of the samples have been investigated with UV-VIS spectroscopy. The setup used in this research is an Agilent Cary 5000 setup. Spectra were taken from 200nm to 860nm wavelengths for both transmission $T(\lambda)$ and reflection $R(\lambda)$ measurements. From here the absorptance is calculated as

$$A(\lambda) = 1 - R(\lambda) - T(\lambda). \tag{3.7}$$

For small wavelengths the glass is not transparent, but its absorptance can also be calculated by Equation 3.7. It is therefore necessary to compensate for the absorption of the glass. This can be done by measuring a glass sample and subtracting this value from the sample absorption measurements. Knowing the thickness of the thin film layer d, the absorption coefficient in the transparent region of the glass can be calculated as

$$\alpha = \frac{1}{d} \cdot \ln \frac{1 - R(\lambda)}{T(\lambda)}. \tag{3.8}$$

The absorption coefficient is useful in determining the bandgap of the material with Tauc plots, as seen in section 4.3.4. UV-VIS provides an alternative in checking the optical properties to SE, so large set-up errors can be found and prevented.

3.2.3 Hall Measurements

The electrical properties of the samples have been characterized by Hall measurements. The working principle of this technique is the Lorentz force, $\vec{F}_{Lorentz} = q(\vec{E} + \vec{v} \times \vec{B})$, where $\vec{E}$ is the electric field, q the electric charge, $\vec{v}$ the particle velocity and $\vec{B}$ the magnetic field. When an electric charge along an electric field moves at a certain velocity in the presence of a magnetic field, it will experience a perpendicular force. In a semiconductor thin film under a perpendicular magnetic field this effect causes the electrons to shift to one side leading to a potential drop called the Hall voltage V_H

$$V_H = \frac{IB}{qnd}. \tag{3.9}$$

Here I is the current passing through the film, B the magnetic field strength, n the carrier density and d the thickness of the film. Note that both electrons and holes are deflected in the same direction by the Lorentz force due to the drift velocities being opposite. As a result the Hall voltage being positive or negative indicates the majority carrier type.

The resistivity ρ of the thin films can be determined by the Van der Pauw technique. By applying a current on each side of a square sample , in both directions, and measuring the potential difference at the opposite site the characteristic resistances R_a and R_b can be determined. The sheet resistance R_S can hereafter be determined by numerically solving the van der Pauw equation

$$e^{-\frac{\pi R_a}{R_S}} + e^{-\frac{\pi R_b}{R_S}} = 1. \tag{3.10}$$

From here, the resistivity ρ is given by $\rho = R_s d$, which in turn can be used to determine the Hall mobility μ_H

$$\mu_H = \frac{1}{qn\rho}. \tag{3.11}$$

For this research SnOx thin films on glass substrate have been cut into 1cm by 1cm pieces and were measured using a PhysTech RH 2010 Hall measurement system. It was uncertain whether the results would be valid for the used kind of samples, so a second opinion was deemed necessary. Vincent Vandelon and Bart Macco, both affiliated with the PMP research group at the TU/e, performed some Hall measurements for this research on a Lakeshore 8400 Series Hall measurement system. This confirmed the validity of the measurements performed at TNO, although the results were considerably less accurate.

3.2.4 X-ray Photoelectron Spectroscopy

Next, x-ray photoelectron spectroscopy (XPS) is a characterization technique which is used to determine the relative atomic concentrations at the surface region of a sample. It is an ex-situ technique, which irradiates mono-energetic X-rays on the material. The penetration depth is the X-rays is a couple of nanometres. It is possible to produce a depth profile by controlled sputtering of the sample. Hydrogen and helium cannot be detected by XPS.

The X-ray photons can be absorbed by the material, which opens up the possibility for electrons to be emitted form the sample. The kinetic energy of the emitted electrons E_k depends on the binding energy of the electron E_B, the energy of the x-rays $h\nu$ and the spectrometer work function W by the relation

$$E_k = h\nu - E_B - W \tag{3.12}$$

The spectrometer work function W is the sum of the work function of the material and a constant to compensate for energy losses in the detector. Every element has a different electron configuration, so a binding energy spectrum can be used to determine which elements are present. The peak areas in the spectrum relate to the concentrations. Additional information can be obtained form the chemical shift of the peaks, the change in energy due to the atoms chemical environment. Deconvolution of the peaks into separate peaks gives information about the occurrence of different chemical states. For example, the Sn3d$_{5/2}$ peaks of Sn^0, Sn^{2+} and Sn^{4+} are at binding energies of respectively 484.7 eV, 486.2 eV and 486.9 eV[43].The XPS measurements in this research are performed by EAG Eurofins, using a QuanteraSXM from Ulvac-PHI set-up, which uses Al Kα radiation, ($h\nu =$ 1486.6 eV).

3.2.5 X-ray Diffraction

In order to study the crystalline properties and structure of the samples x-ray diffraction (XRD) is used as a characterization method. When a crystalline sample is irradiated with monochromatic X-rays, constructive and destructive interference can occur as the X-rays reflect on the crystal lattice planes. The constructive interference conditions are given by Bragg's law

$$n\lambda = 2d\sin(\theta) \tag{3.13}$$

in which n is an integer for the number of wavelengths λ. For varying amounts of angle θ the conditions are satisfied for different lattice spacings d in polycrystalline materials. From the lattice spacing the lattice orientation can be determined. The relative intensities and locations of the peaks can be compared to a database to gather information about the material composition.

In this work a Philips X'PERT SR 5058 X-Ray Diffractometer is used with grazing incidence settings, specified for small incident angles for the incoming X-rays. Measurements were not performed by the author but were carried out by experts within TNO. The angle is varied from 10°to 110 °and the X-rays are produced by a Cu Kα radiation source with a 0.154 nm wavelength.

3.2.6 Raman Spectroscopy

To complement the XRD measurements in this research Raman spectroscopy is performed. For samples for which XRD does not provide a definite answer about the crystalline nature, Raman spectroscopy is an alternative characterization method. Raman spectroscopy provides information on the vibrational states of a material. The technique is based on utilizing the inelastic Stokes scattering of light to determine the energies of the induced vibrational motions.

The Raman spectroscopy measurements are performed with a Renishaw inVia confocal Raman microscope. An helium-neon laser (632nm, 20mW) and an argon laser (514nm, 50mW) are available on this setup. Spectra were taken with the helium-neon laser over the range of 100-1000 cm^{-1}.

Chapter 4

SALD Process Development and Evaluation

This chapter discusses the growth of SnOx thin films by SALD. The first section discusses briefly the difference between thermal SnOx and plasma-assisted SnOx and whether the growth process can be considered an ALD process. In the second section the growth process is characterized and relevant deposition parameters are evaluated. The last section of this chapter analyses the material properties of the grown layers and compares the samples to a tin monoxide reference sample.

4.1 Plasma-assisted Growth of SnOx

Before the plasma-assisted growth of SnOx by sALD is studied the thermal SnOx process is investigated. Without understanding the standard thermal process it is hard to draw conclusions about the effect of the hydrogen plasma on the properties of the samples and the reaction mechanisms. Therefore, this section starts with the thermal SnOx growth before the plasma-assisted growth will be discussed in more detail.

4.1.1 Thermal SnOx Growth

The thermal SnOx sALD process is based on research performed within TNO and the first objective is to verify whether the growth results obtained in the current study are comparable to those produced in previous research and to compare the results to those found in literature. Initial settings are therefore set the same as the work that was done earlier within the research group and they will be optimized after it is confirmed that the samples are comparable.

For the first experiments thermal SnOx was deposited using the rotary SALD set-up as explained in section 3.1. Thin films were grown at a deposition temperature of 150 °C, with 500/500 sccm TDMASn/dilute N_2 at room temperature and 500/500 sccm H_2O/dilute N_2 at 35 °C as the precursors. The rotation speed of the samples has been varied between 10 and 240 RPM, corresponding to a substrate velocity of 31 mm/s and 754 mm/s in the middle of the deposition area, or an exposure time of 24 to 290 ms. For rotation speeds in the saturated region ($\leq$ 60 RPM) the process was run for 800 cycles resulting in a 50-80 nm thick thin film. For depositions performed with a lower exposure time the number of cycles has been increased to obtain samples of similar thickness.

In Figure 4.1a the GPC of the thermal SnOx process is plotted against the exposure time. A clear distinction between the undersaturated and saturated part of the growth can be seen, with the transition happening around 50-60 ms. After saturation the GPC is on average 0.085 nm per cycle, which is a bit higher than values found in literature. For conventional ALD, Mullings et al. found values of 0.07 nm per cycle at 150 °C[21], Choi et al. 0.08 nm per cycle[23] and Elam et al. 0.06 nm per cycle[19]. TDMASn and water have also been used before for sALD by Hoffman et al., who reported 0.075 nm per cycle[22].

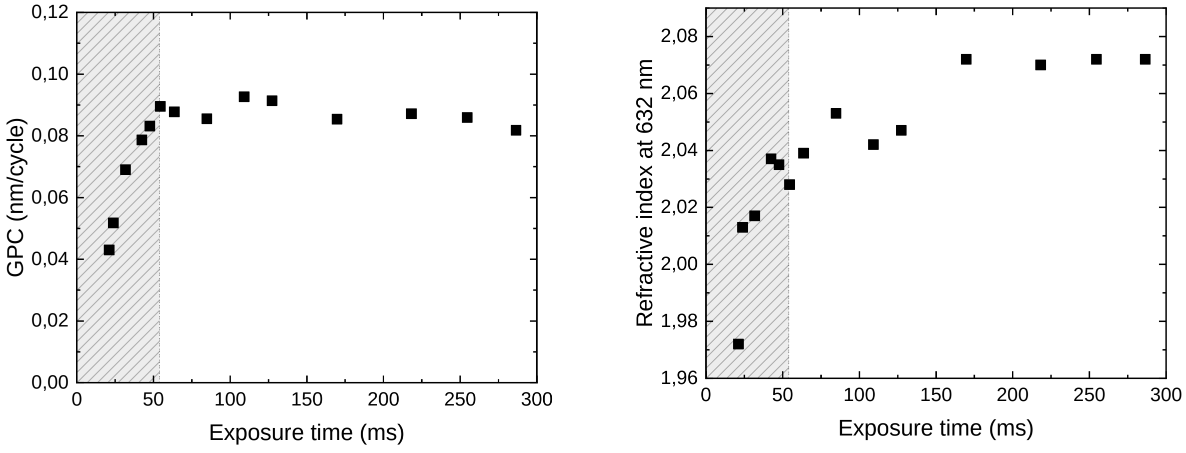

(a) GPC

(b) Refractive index at 632nm

Figure 4.1: The GPC and refractive index of thermal SnOx versus the exposure time. The undersaturated region has been marked with a grey underlay.

The refractive index in Figure 4.1b can be seen to increase slightly at longer exposure times and all data points match the literary values, which vary from 1.95[23] to 2.10[21]. A possible explanation for the higher refractive index at longer exposure times could be increased density of the material, as the thin film layer has more time to fully saturate. This effects levels off at longer exposure times, indicating that an equilibrium has been reached.

As mentioned above, the GPC and refractive index match the results as found literature. These results will function as the reference to where the samples grown with plasma-assisted SnOx will be compared to in order to investigate the effect of adding the plasma as a third step in the ALD process.

4.1.2 Plasma-assisted SnOx Growth

As seen in section 2.2 in the theory, the addition of a hydrogen plasma to the thermal SnOx process should result theoretically in a reduction of the Sn^{4+} to Sn^{2+} or even Sn^0 from which possibly a tin monoxide layer could be grown. In order to study the effect of adding the hydrogen plasma to the deposition process, the growth parameters of the samples are kept identically to those of the thermal SnOx process. The default settings are therefore a 150 °C deposition temperature, 500/500 sccm TDMASn/dilute N_2 at room temperature and 500/500 sccm H_2O/dilute N_2 at 35 °C as the precursors to the process and 800 cycles at a standard deposition speed of 60 RPM. Higher quality films are expected when the plasma step comes after the deposition of the tin, as the plasma will react more to the tin atoms instead of hydroxide ligands on the surface which could possibly shield the tin atoms from the plasma. The direction in which the head rotates is adjusted to this, so the ALD cycle will go as [TDMASn, H_2/N_2 plasma, H_2O] instead of [TDMASn, H_2O, H_2/N_2 plasma]. The plasma will be set to a 2000/8000 sccm H_2/N_2 plasma using a remote SDBD plasma source, as mentioned in section 2.2, set to an alternating current of 125 V at 50 kHz. It should be noted that the plasma injector slot is smaller in size than the precursor injector slots as seen in Figure 3.1, so the average sample will contain both regions where the plasma is and is not applied, as seen in Figure 4.2.

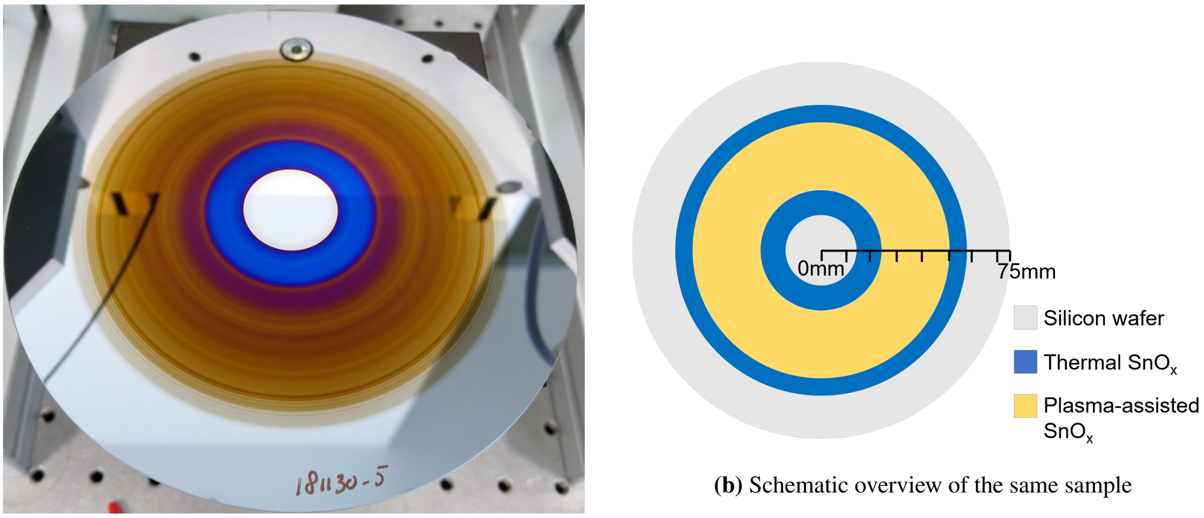

(a) A plasma-assisted SnOx sample

(b) Schematic overview of the same sample

Figure 4.2: An example of a plasma-assisted SnOx sample (a) with a schematic overview of the sample (b) to show the different regions.

A preliminary sample of SnOx deposited at the mentioned standard settings was characterized by spectroscopic ellipsometry as a function of radius and the results are shown in Figure 4.3. At 24 mm a clear drop in thickness and an increase in the refractive index indicate the boundary of the plasma slot, and at 52 mm the deposition goes back to thermal SnOx. This shows that the addition of the plasma for sure changes the material being deposited. From Figure 4.3 it is also decided to take the spots at 15, 30, 35, 40 and 45 mm as the standard measurement locations for all further characterization.

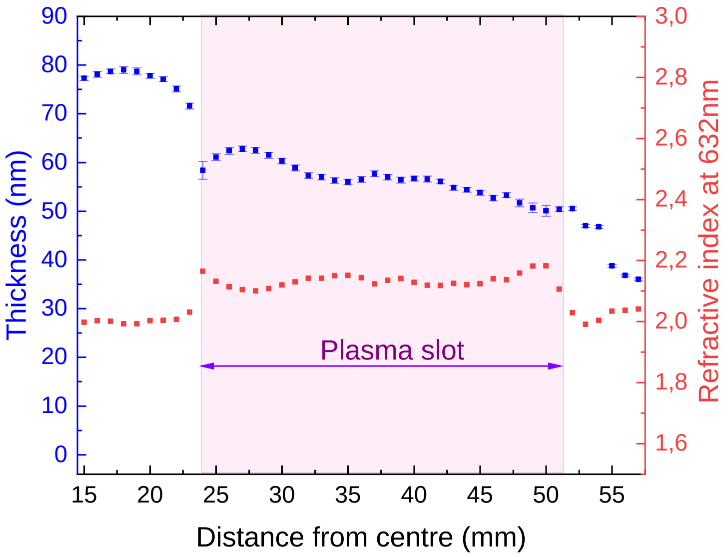

Figure 4.3: An overview of the thickness and refractive index as a function of radius of SnOx deposited on a silicon wafer with a 2000/8000 sccm H_2/N_2 plasma step added. The width of the plasma slot and the precursor injector slots are indicated.

In Figure 4.4 the thickness of the SnOx thin film for the default process is plotted for a varying (200-1600) number of cycles. A clear linear dependence can be seen, which intercepts the (0,0) origin of the axes, indicating that linear growth takes place for this range. Non-linear growth might still be a possibility for a small number (<50) of cycles, but the effect is negligible for the larger number of cycles as used in this research. The refractive index strongly declines with thickness however. This could be a limitation of the spectroscopic ellipsometry model, as in it could be an artefact that happens within the model as the thickness goes to significant lower values than the default 50-80 nm for which the model was calibrated.

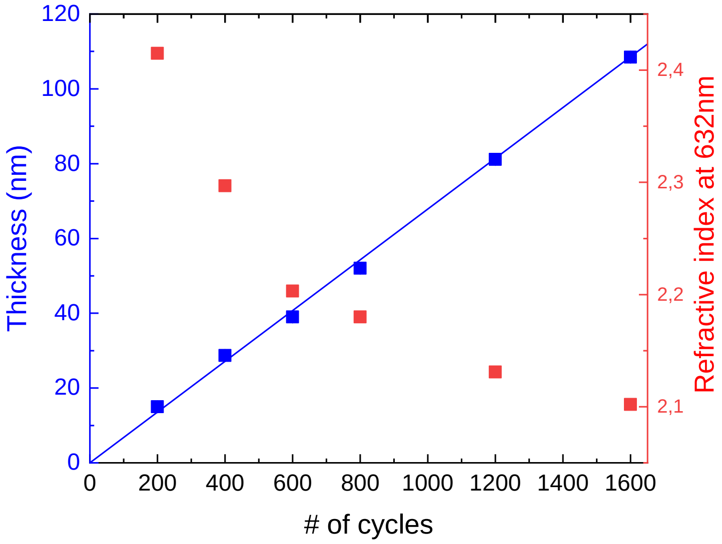

Figure 4.4: The thickness (blue) and refractive index (red) of plasma-assisted SnOx thin film deposition by sALD as a function of the number of cycles. The thickness is fitted with a linear fit, with intercept at (X,Y) = (0,0) corresponding to $Y = (0.0670 \pm 0.0008)X$.

When comparing the plasma-assisted SnOx to the thermal SnOx SALD process in Figure 4.5 some important differences can be observed. The GPC versus the exposure time plots are significantly different, especially in the 50-100 ms region where the thermal SnOx process starts to saturate. The thermal SnOx saturates significantly faster, which is could be an indication of chemical processes happing at a different time-scale compared to the plasma-assisted SnOx. For the latter it could be argued that the process is not fully saturated after 250ms exposure time.

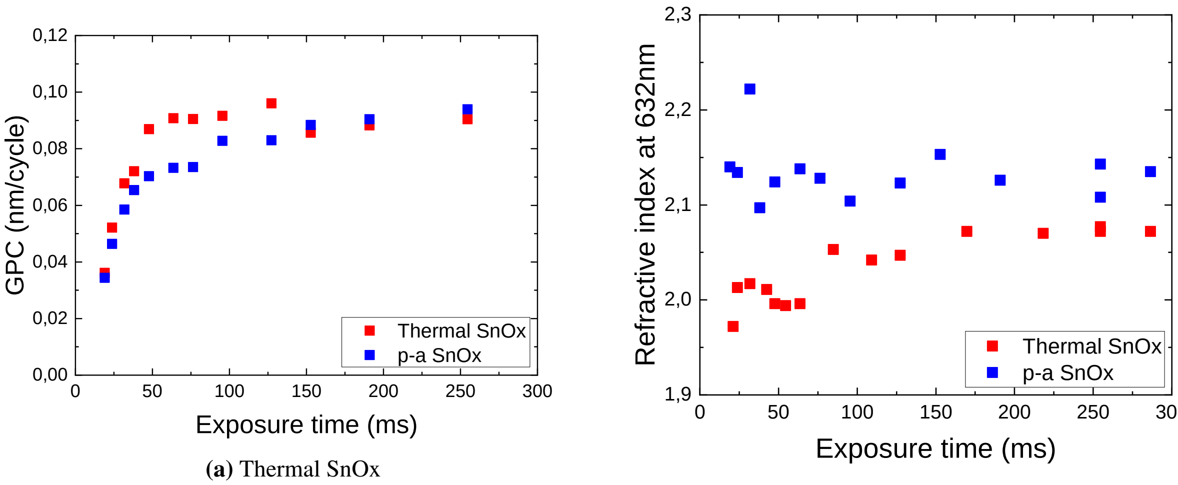

(a) Thermal SnOx

(b) Plasma-assisted SnOx

Figure 4.5: The GPC and refractive index of thermal SnOx and plasma-assisted SnOx SALD depostions at standard settings.

Another important distinction is visible when looking at the refractive index at 632nm. For all exposure times, the refractive index of the plasma-assisted process is significantly higher. This could have multiple causes, such as the density being slightly higher due to an increased amount of vacant spaces in the material and an increase in surface roughness[24], or the material containing some SnO instead of SnO_2. Tin monoxide has a much higher refractive index (2.5-2.8) than tin dioxide (1.8-2.1), so the deposited layer being a mixture of the two materials could explain the difference. Alternatively the plasma-assisted SnOx process could result in a higher density material.

4.2 Process Evaluation

In this section the plasma-assisted SnOx process is studied in more detail. First the effect of the order of application of the precursors, TDMASn-H_2O-plasma versus TDMASn-plasma-H_2O, is investigated and the default precursor order is determined. Subsequently the reproducibility will be established and the growth rate of plasma-assisted SnOx and thermal SnOx will be placed in context. Afterwards multiple process parameters such as the TDMASn, H_2O flow and plasma composition are varied to study their influence and finally the temperature-dependence of the depositions is identified.

4.2.1 Precursor Order

Conventional ALD is based on the reaction of one precursor with one co-reactant, with purging steps in between the application of the steps. The order of application does not matter, as a repeating pattern of A-B-A-B-... is the same as B-A-B-A-... in practice. However, for a three step process such as the plasma-assisted SnOx SALD process there are two different operating modes, with a different precursor order. In this case, the order of application A-B-C-A-B-C-... is not equal to A-C-B-A-C-B-... and whether the plasma step comes after the tin precursor or the water might have implications for the growth. Different chemical processes that might take place and the design of the reactor head in Figure 4.6 results in different purging times between the TDMASn and the H_2O depending on the direction, as additional purging takes place at the plasma slot. The latter could also possibly influence the thermal SnOx process.

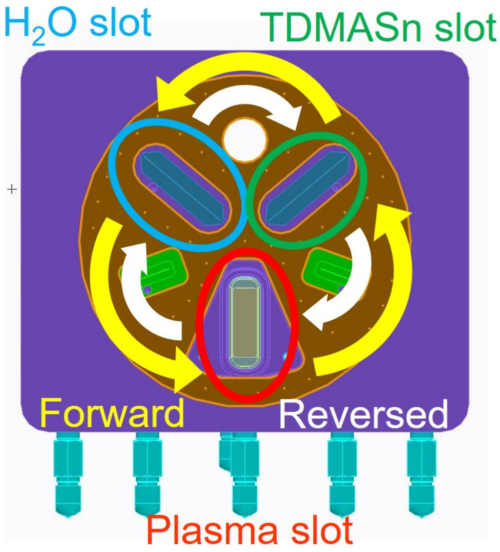

Figure 4.6: A schematic to show the difference in precursor order between the Forward [TDMASn, H_2O (, plasma)] and Reversed [TDMASn, (plasma,) H_2O] operating mode of the POP1 set-up.

An exposure time versus the GPC series is made for both the thermal and the plasma-assisted SnOx process. The results are presented in Figure 4.7. As expected, the thermal SnOx curves do not differ a lot. The difference for this process is whether the longer purge time comes after the TDMASn or the H_2O, and the set-up of the machine should ensure a proper purge. One thing to notice however is that for thermal SnOx in the reversed direction (blue) an overshoot is observed; the GPC at approximately 50 ms is higher than the saturation GPC at longer exposure times. This peculiar observation will be further discussed in section 4.2.3.

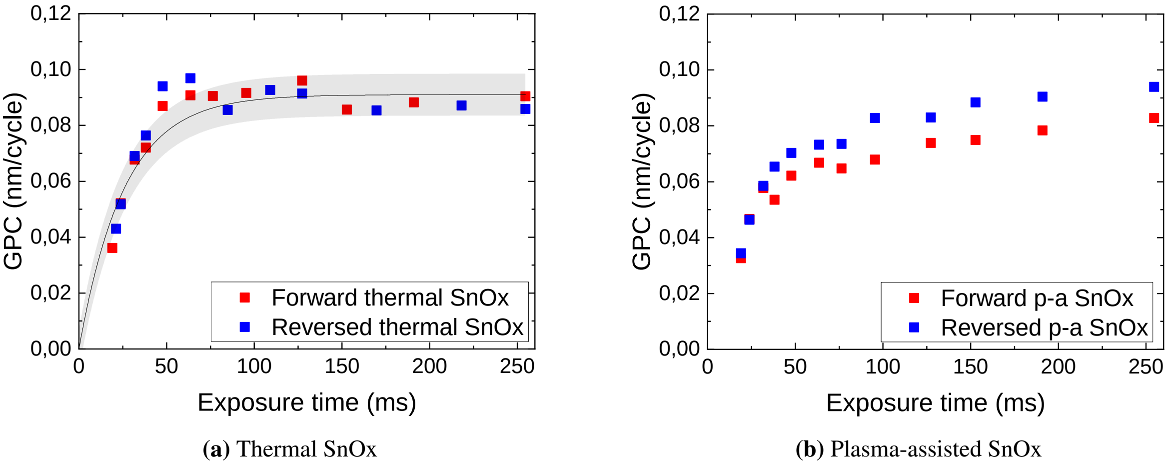

(a) Thermal SnOx

(b) Plasma-assisted SnOx

Figure 4.7: The GPC as a function of the exposure time for thermal and plasma-assisted SnOx processes in the Forward [TDMASn, H_2O(, plasma)] and Reversed [TDMASn (, plasma), H_2O] rotation directions. For the thermal process, a simple fit (Equation 2.7)with a 95% prediction band is added as a guide to the eye. From here it can be seen that the data points for the Reversed direction are unlikely, they overshoot the general trend.

The plasma-assisted SnOx process shows quite a significant difference of up to 30% in the GPC between the Forward and Reversed rotation directions. The fact that this difference is so significant while this is not the case for thermal SnOx indicates that the plasma influences the chemical reactions taking place. It could be an indication that in either of the direction the Sn^{4+} is reduced more than the other, resulting in possible more metallic Sn or SnO than the other direction. It is likely that the Reversed direction would reduce the tin more, as the plasma comes after the TDMASn so slightly more Sn can be considered at the surface where the plasma would be most effective. The saturation GPC for the Reversed direction is also higher than that of the thermal SnOx while the saturation GPC of the Forward direction is comparable, another indication of a different material being deposited.

4.2.2 Reproducibility

In order to establish typical characteristics of the plasma-assisted SnOx deposition process it must be checked whether the discovered results are reproducible. During the course of this research multiple samples have been grown under the same condition, to for example check whether the set-up had been installed properly. These conditions are the standard conditions mentioned in section 3.1, that is 150 °C deposition temperature, 500/500 sccm TDMASn precursor at room temperature, 500/500 sccm H_2O at 35 °C and 2000/8000 sccm H_2/N_2 indirect plasma at 125 V and 50 kHz, all rotating at 60 RPM in the Reversed [TDMASn, plasma, H_2O] rotation direction for 800 cycles. The SE results of these samples are found below in Figure 4.8.

In Figure 4.8a it can be seen that most samples agree reasonably well with one-another, with sample 190115-00 being an outlier. The average spread is around ± 2 nm, which translates to about ± 0.0025 nm/cycle, or ± 4%. Although not ideal, it shows that moderately accurate predictions can be made when a new sample is deposited. For the refractive index in Figure 4.8a an uncertainty of ± 0.03 can be expected. Although a spread of 0.06 can be considered a lot, it is enough to distinguish the plasma-assisted SnOx samples with a refractive index of 2.1-2.15 from the thermal SnOx, which typically have a refractive index of 2.0.

There are several possible reasons for the spread. As seen in Figure 4.3, even within a sample significant

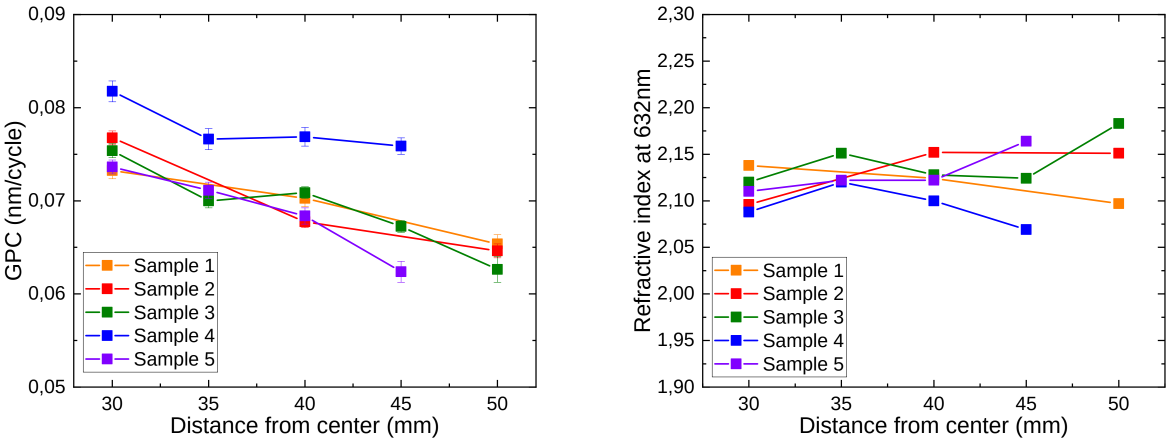

(a) GPC **(b)** Refractive index

Figure 4.8: An overview the GPC and refractive index of multiple plasma-assisted SnOx samples at standard settings produced between November 2018 and February 2019 to show the reproducibility.

derivations from the average value can occur. These could be due to the flow of the precursors, notably are the partial pressures slightly higher at the outlets of the precursors than around other areas, and the partial pressures also change at the edges of the plasma slot. The plasma source itself changes slightly from day-to-day, with the resulting set-up current varying between 0.40 and 0.45 A for the 125 V at 50 kHz settings. There are also some environmental factors which influence the system. The difference between a deposition at the start of the day or the middle, or the end can be noticed as the set-up heats up during the depositions. The depositions that happened beforehand can have an influence as well, as they result in some residue left in the lines. All- things considered, the reproducibility can be considered to be sufficient.

4.2.3 Growth Rate

A common mistake that is made when people learn about ALD is the assumption that an ALD cycle should lead to the growth of one monolayer of the desired material. In real ALD processes, the GPC is less than a monolayer due to for example steric hindrance. The ligands of the absorbed species can be large enough for precursor molecules to be blocked from reaching possible reaction sites[44]. In addition to this factors like the incorporation of impurities, dehydroxylation and imperfect saturation due to insufficient reactivity of the precursors all also affect the growth rate.

Although in-situ measurements where not possible, information about the growth process can be obtained by fitting the data of the thermal and plasma-assisted SnOx against the absorption model introduced in Section 2.3. The GPC versus the exposure time curves for the Reversed rotation direction are shown in Figure 4.9. Hoffman et al.[22] applied the basic model on thermal SALD SnOx and SALD SnOx made with an oxygen plasma, and found their best fits for satisfying results for this model which is shown as the red lines in Figure 4.9. The result for this research are rather unsatisfying, so this model will be reviewed for both thermal and plasma-assisted SnOx.

Thermal SnOx

In Figure 4.9a it is shown that for measurements of thermal SnOx in the Reversed direction, a significant overshoot effect is seen as discussed in section 4.2.1. For the Reversed rotation direction a smaller purge time is present between the water and TDMASn than the other way around. The GPC increases between 50 and 150 ms exposure time, before settling down at a slightly lower rate. Similar additional growth has been described in literature for other processes. Matero et al.[39] attributed the additional growth observed for an ALD process using trimethylaluminium (TMA) and H_2O to increased density of hydroxyl groups remaining on the film surface after the water pulse for large water (10^{-4} g/cycle for a 15cm Si wafer) doses. Following-up on this research, Henn-Lecordier et al.[45] went on to produce a more detailed description of the mechanics and hydrogen-bonding is called out as a plausible process. Hydrogen-bonding of water involves weak chemical bonds between hydrogen and oxygen in the order of 0.2 eV and the bipolar behaviour of water could cause additional water molecules to bond to the substrate surface. As the purpose of purging is the complete removal of any excess adsorbed water, this additional bonding could result to the purge time in the reactor being too short.

Calculations by Tanskanen et al.[27] show that the energetics for the TDMASn reaction with surface OH groups are similar to those with H_2O molecules[46]. Therefore, the TDMASn can react with hydroxide groups as well as physisorbed water molecules. This could result in additional CVD growth in addition to the ALD process.

Maydannik et al.[47] expanded on this idea and they derived a simple model which could provide a good approximation to the observed behaviour. The bonding between water molecules and the surface happen in two stages. First the H_2O molecules react to the surface and terminate the reactive sites to form a monolayer of chemically bonded water. Once the surface is saturated with hydroxyl groups additional water molecules can physisorb by hydrogen-bonding to form a multilayer of absorbed water. When the purge times are insufficient, more water molecules will arrive at the TDMASn precursor head to undergo a reaction. For the thermal SnOx process there is more purge time between the water and the TDMASn in the forward direction than in the reversed direction, which would explain why the excess growth effect is more pronounced in Figure 4.7a for the reversed direction. This effect can be modelled by adding an additional growth term ΔG to the standard simple fit model, its value will be derived below.

For the model, the final thickness of the multilayer depends on two factors, the arrival of water molecules and their rate of desorption. The latter depends on the surface concentration on adsorbed water $Q(t)$ and the probability that the molecules will desorb. According to the Boltzmann equation the desorption rate R_d is given by

$$R_d = L\exp(-\frac{E}{kT}) \tag{4.1}$$

with L a constant including the molecular vibration frequency, E the molecular binding energy (eV), k is Boltzmann's constant (JK^{-1}) and T the temperature in Kelvin. The rate of water molecules accumulation is described by a simple first-order linear differential equation

$$\frac{dQ(t)}{dt} = IS - Q(t)R_d \tag{4.2}$$

where $Q(t)$ is the surface concentration, S sticking coefficient and I impingement rate of water. The latter two are functions of the water partial pressure and the temperature, which will be kept as a constant for the samples, so we can write variables as a single constant $b = IS$. The global solution to the differential equation is

$$Q(t) = b\tau + c\exp(\frac{t}{\tau}) \tag{4.3}$$

where $\tau = \frac{1}{R_D}$ is a time constant and c an integration constant. Assuming the boundary condition that the surface concentration at the start of the process is zero, $Q(0) = 0$, c can be solved for to obtain

$$Q(t) = b\tau(1 - \exp(\frac{t}{\tau})) \tag{4.4}$$

The surface concentration of adsorbed water $Q(t)$ will be limited by the residence time in the water precursor slot zone. As the substrate then rotates through the purge zone, it will desorb water in a thermally activated way such that the amount of water remaining on the substrate at the tin precursor slot $Q_{Sn}(t)$ is given by

$$Q_{Sn}(t) = Q(t)\exp(-\frac{t_p}{\tau}) \tag{4.5}$$

where t_p is also the time the substrate spends in the purge zone each cycle and τ the same as defined above. Although the purge times and the exposure times for the precursor slot aren't necessarily equal, they are approximately equal due to a constant rotation speed of the sample and will therefore be considered the same, so $t_p = t$, for the simplicity of the model. The excess growth $\Delta G(t)$ will be dependant on the amount of water remaining on the surface after purging multiplied by a constant factor which relates the amount of reacted material to the resulting growth in nm c, which will be incorporated in constant fitting term b as

$$\Delta G(t) = cQ_{Sn}(t) = bQ(t)\exp(-\frac{t}{\tau}) = b\tau(1 - \exp(-\frac{t}{\tau}))\exp(-\frac{t}{\tau}) \tag{4.6}$$

This excess growth will be added to the default exponential model for the GPC versus exposure time of the SALD processes to acquire an significant improvement in the fit as seen in Figure 4.9a.

The model compensates for additional growth in a small region of the exposure time range, as for small exposure times the term $(1 - \exp(-\frac{t}{\tau}))$ reduces to zero, while the last part $\exp(-\frac{t}{\tau})$ does the same for large exposure times. Physically this makes sense, as there is either not enough time for water molecules stick to the surface by physisorption, or an increase in the exposure time leads to larger purge times which would effectively remove the additional water.

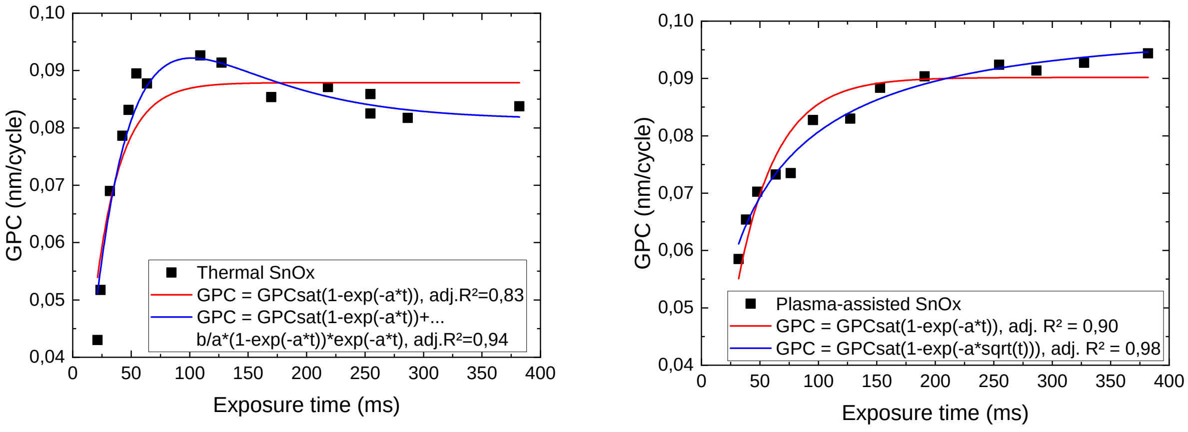

(a) Thermal SnOx

(b) Plasma-assisted SnOx

Figure 4.9: The GPC versus the exposure time fitted for thermal and plasma-assisted SnOx. The red line represents the standard saturation curve $GPC = GPC_{sat}(1 - \exp(-a \cdot t))$, the blue lines show the best fitting model.

Plasma-assisted SnOx

The model which compensates for the physisorption of water mentioned above does not work for the plasma-assisted SnOx depositions in Figure 4.9b. Here no overshoot of the GPC is present and the data shows a soft saturation curve. Although the increase in GPC levels off, even after long 300+ ms exposure times the curve cannot be considered fully saturated. When fitted with a standard exponential function (red) it becomes clear that the time dependency of the equation must be adjusted or another term must be added which influences the growth at longer exposure times. Therefore it can be concluded that water film effects do not play a role in the plasma-assisted SnOx process. This hints towards another rate-limiting reaction step for this ALD process compared to the thermal SnOx process. To investigate the possible effects happening, the basic model is compared to four other fitting models below.

The first is the possibility of parasitic CVD growth, which adds a linear term $+c \cdot t$ with c a constant which describes the CVD growth rate to the original equation. The addition of this term would cause GPC to infinitely increase with exposure time, so this model could be confirmed or debunked by producing samples at extreme exposure times ($>>$400ms), which is not possible at the current set-up. This model provides a better fit to the data, but feels like a sub-par solution as its CVD deposition rate constant c changing an huge amount depending on the maximum exposure time, and with that the predicted GPC_{sat}.

The next model is the possibility of two different chemical processes taking place with comparable time constants, which both increase the GPC and are independent of each other. The addition to the basic model is $+GPC_{sat2} * (1 - \exp(-b * t))$, with GPC_{sat2} and b comparable constants to those in the basic model itself. The disadvantage of such a model is overfitting, as the same effect is accounted for twice and the constant could be used interchangeably. As expected, this model is unable to fit due to a lack of data, and although the fit does not converge it produces a reasonable assumption, but the parameters correlate too much to provide additional information.

The third model that provides a better fit is the diffusion limited mass transport model, which changes the time-dependency in equation 2.7 to $-a\sqrt{t}$. The basis for the square-root dependency is assumed to be the case that the growth rate of the reaction is limited by the diffusion of the precursor through the diffusion boundary layer to the substrate. This effect has been found to exist for ZnO[48,32] and AlOx by Poodt et al.[12]. They found for SALD under similar circumstances that for the AlOx process the assumed surface coverage θ scales with $\exp(-a\sqrt{t})$ and provided a possible explanation. For a flux of precursor molecules towards a substrate Fick's laws of diffusion can be solved to give a time-dependent concentration gradient, where the concentration or partial pressure scales with $\exp(-a\sqrt{t})$. This model fits particularly well, and predicts the cause of the rate-limiting behaviour of the being in the reactor design and set-up instead of being a fundamental property of the reaction itself. The results could therefore be different in another set-up, which limits the scalability of the process. Furthermore, it does not provide any additional information for cases when the precursor dose is changed.

For the final model, the assumption is made that the growth is fully limited by the amount of precursor dosed to the substrate and thus the exposure time is a function of dose instead of the time it takes for the chemical reaction to occur. The exposure time is converted to the SPD according to Equation 2.8. Subsequently the data is fitted with the model in Equation 2.10. This model with two adjustable parameters produces a fit which rivals the diffusion-limited model in accuracy with an adj. R^2 value of 0.97. It also has the ability to predict behaviour under varying precursors flow, which will be covered in the next section.

An overview of the fits from these various models are shown in Table 4.1 below. Curiously, the two best-fitting models, the diffusion-limited and dosage-limited model, both assume the growth-limiting process as a function of the exposure time to not be due to the chemical reaction rate. Both models provide restrictions on the amount of precursor that reaches the substrate instead. Therefore it can be concluded that the GPC of the plasma-assisted SnOx process, in contrast to the thermal SnOx process, is not influenced by the amount of water as a co-reactant, but limited solely by the amount of TDMASn precursor.

Table 4.1: An overview of different models which can be used to describe the GPC as a function of the exposure time for plasma-assisted SnOxs

Model name	Formula, $GPC(t) =$	# of parameters	adj. R^2
Basic	$GPC_{sat} \cdot (1 - \exp(-a \cdot t))$	2	0.90
Linear CVD	$GPC_{sat} \cdot (1 - \exp(-a \cdot t)) + c \cdot t$	3	0.95
Two-step process	$GPC_{sat1} \cdot (1 - \exp(-a \cdot t))$ $+GPC_{sat2} \cdot (1 - \exp(-c \cdot t))$	4	Unable to converge.
Diffusion-limited	$GPC_{sat} \cdot (1 - \exp(-a \cdot \sqrt{t}))$	2	0.98
Dosage-limited	$GPC_{sat} \cdot \frac{K \cdot SPD(t)}{1+K \cdot SPD(t)}$	2	0.97

4.2.4 Precursor Dependency

In the previous section it was theorized that the GPC of the plasma-assisted SnOx process is to a significant degree dependent on solely the amount of TDMASn added. In order to investigate this, an experiment was performed where the amount of carrier gas flowing through the TDMASn bubbler was decreased from 500 sccm to 50 sccm, lowering the TDMASn partial pressure from 0.08 mbar to 0.008 mbar. The SE results are given in Figure 4.10. Two different exposure times where chosen at 42ms and 64ms, which are just before and just after the exposure time at which the reaction saturates under standard conditions.

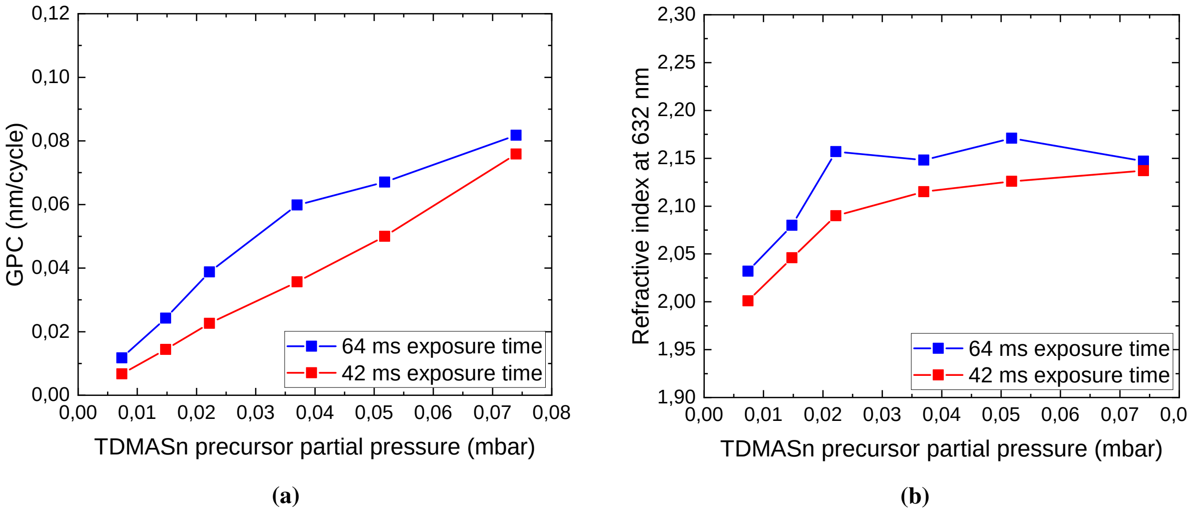

(a) **(b)**

Figure 4.10: The (a) GPC and (b) refractive index of plasma-assisted SnOx for varying TDMASn partial pressures at 42 and 64 ms exposure time.

In Figure 4.10a the GPC is plotted for an exposure time of 42 ms and 64 ms. The GPC scales approximately linear with the TDMASn partial pressure for an exposure time of 42 ms. This indicates that the growth is limited solely by the amount of TDMASn that reaches the surface. The refractive index in Figure 4.10b also increases with a higher partial pressure, but saturation starts at a partial pressure of 0.04 mbar.

As the number of molecules that reach the surface is not only dependant on the partial pressure, but also on the exposure time, it is expected that for a longer exposure time saturation takes place at a lower pressure. This is visible in Figure 4.10a for an exposure time of 64 ms, where the GPC versus partial pressure is not linear over the whole range, but saturation in the growth can be seen at partial pressures higher than 0.04 mbar. The refractive index is even at 0.02 mbar already at it's maximum value. This exposure time dependency shows that the reaction is limited by the dosage of TDMASn precursor, so it should be expected that the amount of H_2O added to the reaction does not make a difference at short exposure times.

With the assumption that the growth of the reaction is limited by the amount of precursor molecules entering the system, it is useful to check the GPC versus the TDMASn exposure in SPD as explained in section 4.2.3. Figure 4.11 shows the GPC versus the SPD for different amounts of flow through the TDMASn bubbler. For reference the dosage-limited fit from that section is also added.

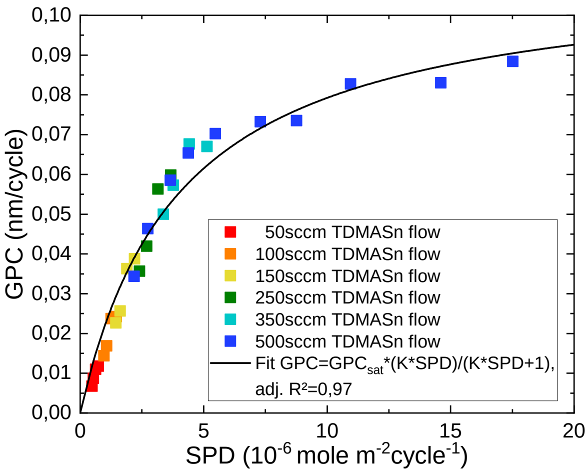

Figure 4.11: The GPC plotted against specific precursor dosage of TDMASn, which are calculated with TDMASn partial pressure and the exposure time.

From the figure it can be seen that the SPD provides an excellent parameter to summarize bubbler flow and exposure time in a single parameter. If they were unrelated, multiple trends would have been visible instead of a single trend. In this research no experiments with varying bubbler temperatures, which alter the precursor partial pressure, have been performed. For follow-up research it would be interesting to test the SPD parameter against this data.

The fit provides an adequate explanation for the data, functioning at both high and low doses. For a critical note however, going from low to high SPD the model overestimates, underestimates and again overestimates the GPC. For a proper model the residuals of the data (the data values minus the fit) should be random instead of correlated. Therefore, some important parameter in the data is currently unaccounted for.

In fact, the data could be interpreted as two different regions. The GPC follow a linear relationship up to $4*10^{-}6$ (mol^{-2}m^{-2}cycle^{-1}) of TDMASn, after which for higher values saturation takes place. It is uncertain whether this is an artefact of the data collection, with the 500 sccm flow measurements being performed at another day. Alternatively an SPD of $4*10^{-}6$ (mol^{-2}m^{-2}cycle^{-1}) could be a critical value, after which the substrate becomes fully saturated or the diffusion of the precursor to the substrate starts to be limited due to the setup geometry. To further investigate this the refractive index versus the SPD is shown in Figure 4.12 below. The refractive index dropping at lower values could indicate the deposition of a material with a lower density and the growth is not yet saturated. Saturation starts at an SPD of $2*10^{-}6$ (mol^{-2}m^{-2}cycle^{-1}), with values of 2.10-2.15 for the remainder of the SPD range. Therefore for saturated SnOx growth it is necessary to adjust the precursor dose to be well over this value, which corresponds to 18 ms of exposure time, or 20 mm from the centre of a 15 cm Si wafer at 120 RPM, at

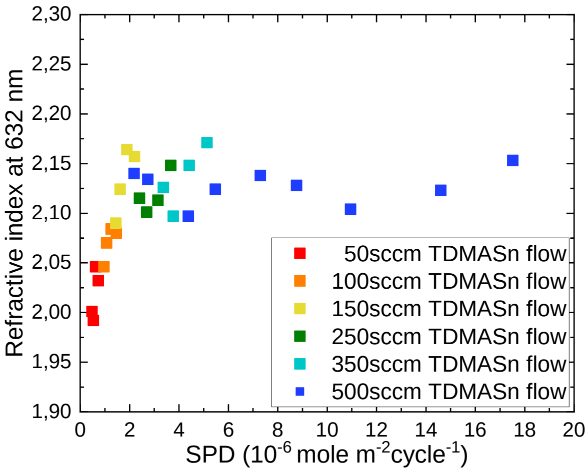

Figure 4.12: The refractive index plotted against specific precursor dosage of TDMASn, which are calculated with TDMASn partial pressure and the exposure time.

500 sccm of flow through the TDMASn bubbler at room temperature.

4.2.5 Co-reactant Dependency

In the previous section a case is made that the growth of plasma-assisted SnOx depends primarily on the amount of TDMASn precursor dosed and is independent of the amount of water added as a co-reactant. As seen in section 4.2.3, the reaction mechanism of thermal SnOx does depend on the behaviour of hydroxyl groups on the sample surface. As this shift in reaction mechanisms was unexpected, it was further investigated by varying the water dosage.

A measurement series was made consisting of plasma-assisted SnOx samples under standard conditions, with varying amounts of water. Changing the flow through the water bubbler from 500 sccm to 100-1000 sccm and changing the water temperature between 5 °C and 50 °C results in a dataset range of H_2O partial pressures from 1 mbar to 150 mbar, as shown in Figure 4.13.

For most of the partial pressure range, the GPC and refractive index stay approximately the same. The refractive index drops for 1 mbar of partial pressure to 2.0, which is comparable to samples of thermal SnOx. It is hard to say what the significance of the data is without knowing what the effect of lowering the partial pressure even more is. The extreme case is a deposition without adding water, which will be covered in section 4.2.8. As the range in which the partial pressure is varied is quite large without significant effects, it can be concluded that the amount of water added to the system is not a significant parameter and even low amounts are already sufficient for growth to take place. Even though the reaction takes place at an exposure time which is still unsaturated, the GPC is not limited due to the amount of water partial pressure.

4.2.6 Plasma Composition

As discussed in previous sections of this chapter, the usage of a H_2/N_2 plasma for the growth of SnOx by sALD increases the refractive index, which might indicate the presence of tin monoxide in the layer, and changes the rate-limiting behaviour of the reaction to change from the OH surface groups to the TDMASn exposure. In order to further investigate the effect of the H_2/N_2 plasma, the composition is

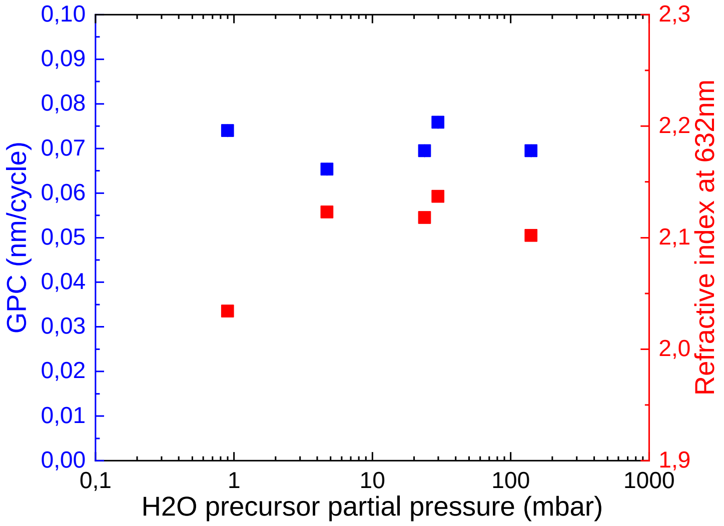

Figure 4.13: The GPC and refractive index of plasma-assisted SnOx for varying H_2O partial pressures at 42 ms exposure time.

varied to see whether the effect results from the addition of a plasma, or more specifically the hydrogen plasma as theorized in section 2.2. As said it has already been shown that the addition of a H_2/N_2 has an effect on the sample properties, but it is not yet clear whether this is the result of the hydrogen or the nitrogen plasma. As theorized in section 4.2.1, a possible effect of the plasma could be the removal of hydroxide ligands from the sample surface, which possibly would also be possible with just a N_2 plasma. In that case a pure N_2 plasma should yield the same properties as the mixture. The result can be seen in Figure 4.14. The total plasma flow is kept constant at 10 slm, but the composition is varied from 0/10 slm H_2/N_2 to 2/8 slm H_2/N_2

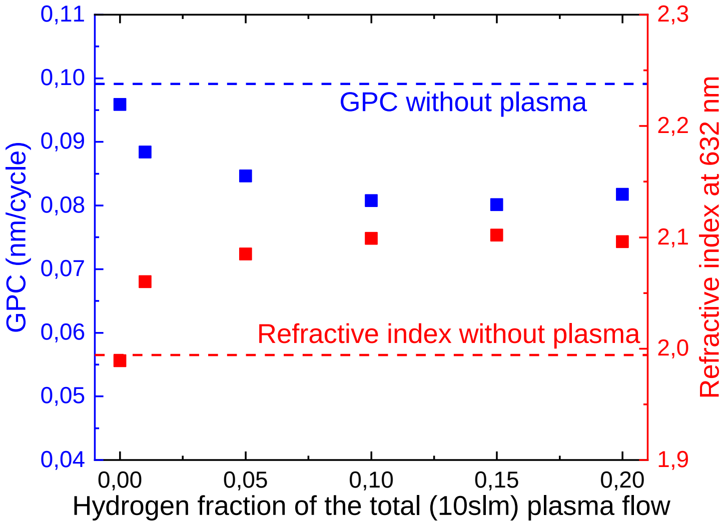

Figure 4.14: The GPC and the refractive index of plasma-assisted SnOx sALD depositions as a function as the amount of hydrogen added to the nitrogen in the plasma.The total plasma flow is kept constant at 10 slm.

As the GPC and the refractive index show, the nitrogen plasma has little influence on the process and the hydrogen plasma is the cause of the beforehand mentioned reaction behaviour change. For a pure nitrogen plasma these values stay approximately equal and the effect grows significantly for small amounts of hydrogen added, until saturation takes place around 1000/9000 sccm H_2/N_2 and both the GPC and the refractive index stay constant for larger amounts of hydrogen. This saturating behaviour is a strong indicator of a chemical reaction between the hydrogen plasma and the thin film layer.

An undesirable side effect of using a plasma could be the etching of the thin film layer. If the hydrogen plasma were to etch the sample, it would be expected that a change from 1000 sccm to 2000 sccm would also result in a drop in the GPC, but this is not the case. Therefore etching effects due to the hydrogen plasma are not present.

4.2.7 Deposition Temperature

For ALD processes to occur, the deposition temperature needs to be within a certain range. For temperatures below this range unwanted mechanisms as precursor condensation and incomplete reactions lead to unwanted CVD-like growth and produce poor-quality thin films. The same goes for temperatures above this range, as the precursor decomposition and thermal desorption will lead to impurities and reduced growth. For tin oxide processes and the TDMASn precursor a temperature dependency has been shown in literature[21]. To the check whether the processes described in this report are comparable, depositions have been done at four different deposition temperatures as shown in Figure 4.15.

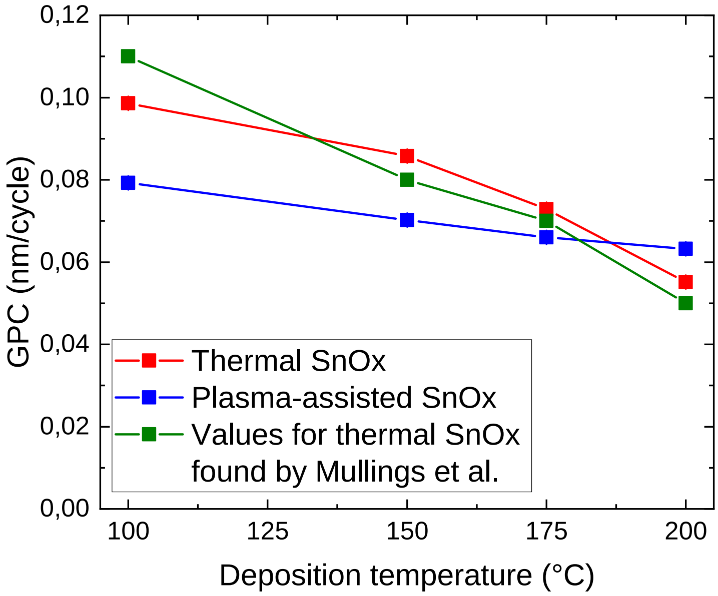

Figure 4.15: The growth per cycle at an exposure time of 48 ms for different deposition temperatures. It can be seen that the effect of increasing the deposition temperature is larger for thermal SnOx than for plasma-assisted SnOx. For comparison, values for thermal non-spatial SnOx found by Mullings et al.[21] are added in green.

In Figure 4.15 it can be seen that the processes with and without plasma have a different temperature dependence. For thermal SnOx the GPC goes down faster with increasing temperature than for the plasma-assisted SnOx process, which with a difference in GPC of 0.01 nm/cycle can almost assumed to be constant. The GPC values for thermal SnOx correspond well to the values found by Mullings et al.[21] for a non-spatial ALD process, with values of 0.11, 0.08, 0.07 and 0.05 nm/cycle for deposition temperatures of respectively 100, 150, 175 and 200 °C. These values are added to Figure 4.15 in green.

In previous sections it had been shown that the GPC as a function of the exposure time is different for the thermal and plasma-assisted SnOx process. Data as in Figure 4.15 which is dependent on one specific exposure time might therefore skew the data. In Figure 4.16 the deposition temperature dependency for both processes is shown for a range of exposure times.

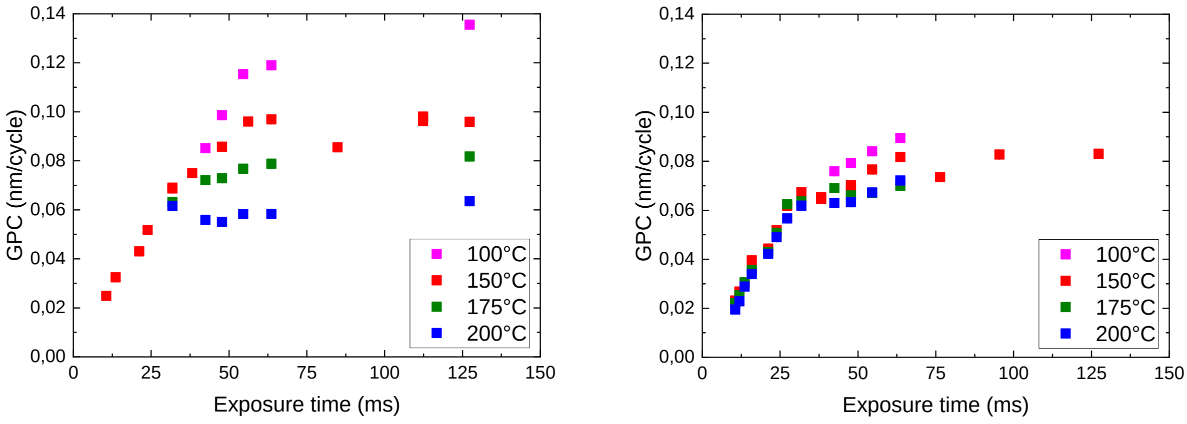

(a) Thermal SnOx

(b) Plasma-assisted SnOx

Figure 4.16: The GPC as a function of the exposure time thermal and plasma-assisted SnOx at different deposition temperatures.

Figure 4.16 shows excellent evidence for the difference in behaviour between both processes at different deposition temperatures. For the thermal SnOx a large temperature dependency is observed over the whole range of different exposure times, while for plasma-assisted SnOx there is only a slight temperature dependence.

The GPC decrease for higher exposure times is a common phenomenon for ALD from alkyl-amide precursors[44]. A change in the number of reactive surface groups might account for the decreasing GPC. This behaviour has been interpreted for SnOx by precursor condensation[23] or by an increased number of surface hydroxyl groups at lower temperatures[19,44]. The presence of additional water due to physisorption at lower temperatures increase the density of OH reaction sites. Tanskanen et al.[27] have shown neighbouring OH groups on the surface facilitate the water half-reaction as seen in Equation 2.2.

For the plasma-assisted SnOx the temperature dependency is not present, but the amount of physisorpted water added during the co-reactant step in the cycle should be the same as for the thermal process. After all, the amount of physisorption just dependant on the temperature if the chemical reaction were to be the same.

What could be happening instead is the successful reduction of tin by the hydrogen plasma (Equation 2.3), followed by re-oxidation of the sample in the co-reactant step (Equations 2.13 and 2.14). This sequence of reaction would not be so strongly temperature dependent.

4.2.8 Depositions Without Water

In addition to the depositions with varying amounts of water precursor done in section 4.2.5, some depositions have been performed without H_2O as a co-reactant. In principle, an ALD reaction with just a precursor and no co-reactant should not yield any growth. The nitrogen plasma could perform the role of co-reactant, but the significant 100x timescale difference of the process compared to literature[36] should result in just a small amount of growth as explained in section 2.2. The results of these waterless depositions are summarized in Figure 4.17. From this figure a surprising result can be seen, as the GPC for the process without water closely approximates the other processes.

The most likely explanation for this result is the formation of metallic Sn instead of SnO or SnO_2. The hydrogen plasma as explained in section 2.2 in this report reduces the Sn^{4+} to either Sn^{2+} or Sn^0. It

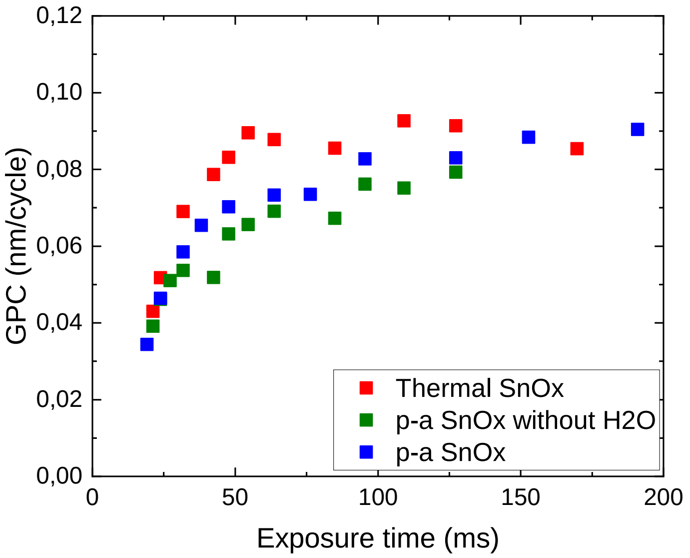

Figure 4.17: The GPC versus the exposure time for the thermal SnOx process, the plasma-assisted (p-a) SnOx and the plasma-assisted SnOx without water process.

could be possible for the TDMASn to bind to Sn^0 surface molecules. This would result in a large amount of tin in the material composition.

The refractive index of this material varies between 2.3 and 2.5, which could be an indicator of the presence of tin monoxide. While oxygen atoms should in theory not be present in the reactor, in practise oxygen and water vapour leaks into the reactor due to the deposition taking place at atmospheric pressure. Some oxygen or water would also be present in the nitrogen used for the plasma and the purging of the reactor. The formation of tin monoxide with this process seems unlikely though due to the extremely low oxygen partial pressure that would be present.

Another possible process is the formation of tin nitride due to the nitrogen plasma. Nitrogen plasma has a low reactivity to TDMASn and very long exposure times in the range of 20-100 seconds are necessary to saturate the surface and remove the methyl ligands[36]. Therefore, tin nitride would not form due to water having an significantly higher reactivity. In the absence of water however tin nitride might be a possibility, but such a high GPC would still be unexpected.

In order to verify the material composition of this process, plasma-assisted SnOx samples without water will be taken into account for most of the characterization methods discussed in the next section.

4.3 Sample Characterization

This section starts of with an overview of the electrical properties of SnOx as a function of the hydrogen-to-nitrogen plasma ratio used in the process. In order to better investigate the material properties with other measurement techniques, reference tin monoxide samples are introduced in the second subsection. The development of these samples happened in parallel to this research and it was possible to obtain some measurement results for accurate comparisons. This is put in practise in the following paragraphs for XPS, XRD, Raman and UV-VIS measurements. Finally, this section will finish with a short investigation into the possibilities of annealing the samples.

4.3.1 Electrical Properties

The main goal of adding the hydrogen plasma to the thermal SnOx process is to see whether it is possible to form a tin monoxide thin film layer, which is a p-type semiconductor instead of n-type for the tin dioxide. One way to check whether a layer is a p-type semiconductor is by performing Hall measurements as explained in section 3.2.3. A measurement series of various SnOx samples with increasing amounts of plasma is made and the results of the Hall measurements are summarized in Table 4.2 below.

Table 4.2: An overview of various electrical properties of plasma-assisted SnOx samples at varying ratios of hydrogen plasma.

Hydrogen ratio plasma	Sheet resistance ($\Omega/\Box$)	Carrier concentration (cm^{-3})	Hall mobility and type ($cm^2\ V^{-1}s^{-1}$), p or n
No plasma	2.28E7	2.0E17	n 0.29
0.01	9.89E3	4.9E19	n 2.46
0.05	6.93E3	5.8E19	n 2.60
0.1	5.64E3	7.6E19	n 2.43
0.15	6.42E3	5.8E19	n 2.80
0.2	6.46 E3	5.9E19	n 2.30

It turns out that even adding the smallest possible amount of hydrogen plasma available for the set-up to the SnOx layer changes the electrical properties drastically. The resistance and sheet resistance of the 1 cm by 1 cm samples drop by 4 orders of magnitude, the carrier concentration multiplies 200 to 400 times and the measured Hall mobility increases tenfold. This research aimed to produce p-type materials, the addition of an hydrogen plasma to the process results in n-type SnOx still. It can also be seen that even though the smallest value of 100 sccm of hydrogen plasma (and 9900 sccm of nitrogen plasma) has a large effect, the effect is not saturated until the addition of 500-1000 sccm of hydrogen plasma. As proposed in section 4.2.1, the cause of this effects could be the the removal of carbon impurities by the plasma, as these drastically lower the carrier concentration[23]. More on this will be discussed in section 4.3.3.

This phenomena has been covered in literature though and the increased electrical conductivity of SnOx has been attributed to the incorporation of hydrogen in the tin oxide[49]. Hydrogen can bond with oxygen in the tin oxide and act as a donor resulting in n-type conductivity[26]. Therefore this is a probable cause to the increase of the electrical properties, although it does not exclude the removal of carbon impurities taking place. The incorporation of hydrogen in the layer is unfortunately unable to be detected with the various techniques used in this research, so this should be incorporated in further research.

4.3.2 Tin Monoxide

The goal of this research is to produce p-type tin monoxide thin film from a tin(IV) sALD precursor. To determine to which degree this goal is accomplished it is helpful to have a SnO reference sample. Fortunately it was possible to obtain reference data from such a sample produced on the same POP1 set-up with the bis[bis(trimethylsilyl)-amino]tin(II) precursor and H_2O. This process succesfully resulted in a p-type material. The temperature dependent saturation GPC and refractive index at 632nm of the tin monoxide can be found in Figure 4.18.

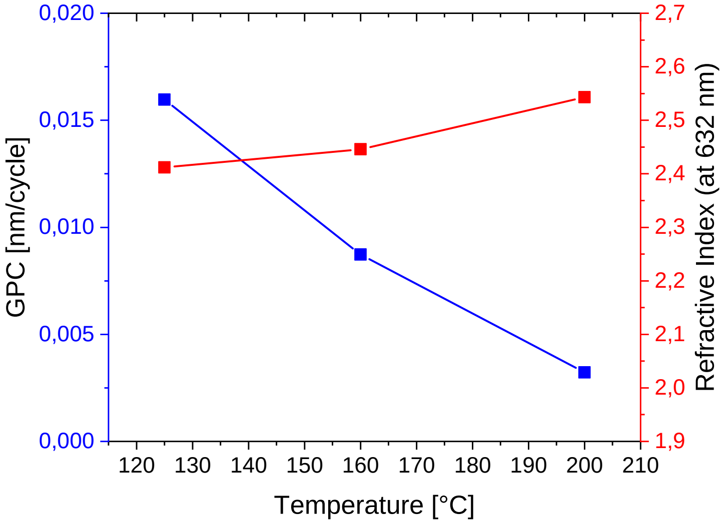

Figure 4.18: The GPC and refractive index of saturated SnO grown with a bis[bis(trimethylsilyl)amino]tin(II) precursor and water at various deposition temperatures.

At a glance, the GPC is significantly lower than the GPC of the TDMASn tin(IV) precursor. Where as the thermal and plasma-assisted SnOx in this research reach values of up to 0.10 nm per cycle, the tin(II) precursor process caps at 0.016 nm per cycle for a deposition temperature of 125 °C and drops to 0.003 nm per cycle for 200 °C. This indicates a different type of process taking place than the temperature-independent plasma-assisted SnOx. It is however hard to say whether the rate-limiting reaction for this process is the same as for the thermal SnOx.

The refractive index is with values of 2.4-2.6 considerably higher than the samples produced in this research, with exception of some plasma-assisted without water SnOx depositions which approach 2.4. The refractive index being this high is a clear indication of a tin monoxide layer being deposited instead of a mixture, which makes the samples very suitable for comparisons with other techniques.

It was not possible to obtain Hall measurement data of the tin monoxide samples, but XRD, XPS, UV-VIS and Raman data was available and will be shown for comparison in the next sections.

4.3.3 Material Composition

XPS

The material composition of the samples is determined by XPS. The XPS characterization is performed by Eurofins EAG, and the samples are checked for Sn, O, N, C and Si. Sputtering is used to obtain a relative depth profile, to check whether the composition changes within the thin film, accounting for preferential sputtering. The distance from the surface is given in nanometres of SiO_2 sputtering equivalent. That is, if the material where SiO_2, the composition would be measured at every nm of depth.

The composition will be compared to the reference SnO sample, which consists of 47.6% oxidized Sn, 10.3% metallic Sn, 41.3% O and 0.8% N. This ratio of O/Sn of 0.72 is very close to values of 0.74 found in literature[15] for SnO. For the other samples however, due to the uncertainty in the data it was not possible to split the tin in a metallic and oxidized part, as the difference in binding energies is just 0.9 eV. The results of the SnOx samples can be found in Figure 4.19.

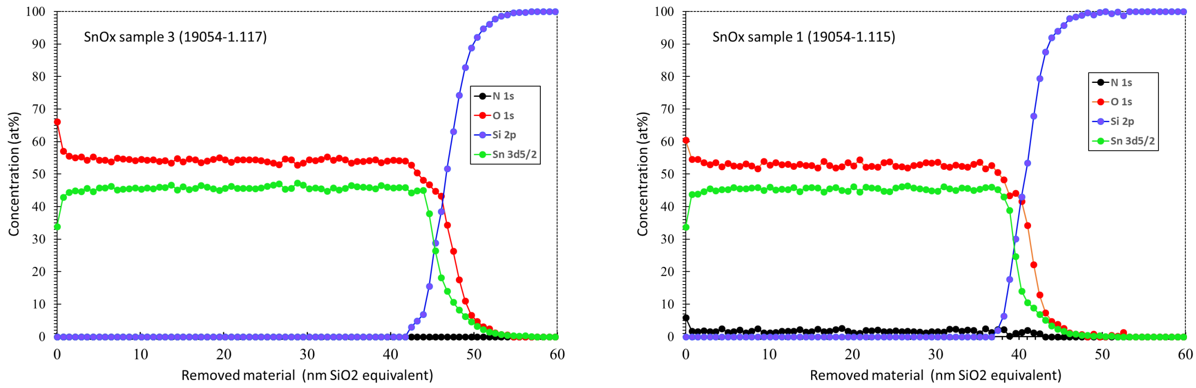

(a) Thermal SnOx

(b) Plasma-assisted SnOx

Figure 4.19: Elemental concentrations of thermal and plasma-assisted SnOx samples as determined by XPS. Measurements are performed at every nm equivalent of SiO_2 sputtering to show the change in composition over the whole layer.

The XPS results of the SnOx samples yield a ratio of about 45:55 of Sn:O, which differs from the 58:41 of the tin monoxide reference. This result is very close to the results obtained for SnO_2 by Kim et al.[15], who also found a relative O:Sn ratio of 1.2 and an uniform O/Sn distribution in the depth direction. It should be noted that the absolute O/Sn ratio determined by XPS analysis is not very accurate even after considering the atomic sensitivity factors of each element. Still, it can be concluded that the samples are close to pure tin dioxide.

Some other interesting things can be noted in Figure 4.19. At the surface the ratio of O:Sn is higher than in the bulk, probably due to surface contamination with CO_2 and H_2O. No carbon is detected in these samples however, so DMA ligands are not broken down in the deposition process. This means that the increased refractive index is probably the cause either an increase in density or local crystallization within the material[50]. For the electrical properties it also implies that the incorporation of hydrogen causes the increase in charge carriers and decrease in sheet resistance.

Although the thermal and plasma-assisted SnOx XPS results are very similar, an important difference can be seen in the amount of nitrogen in the sample. For thermal SnOx this amount is zero, but for plasma-assited SnOx it varies around 2% as seen in Figure 4.20.

A DMA ligand contains both carbon and nitrogen, so the observation of nitrogen within the plasma-assisted SnOx but no carbon is remarkable. It was already concluded that the DMA ligands are not broken down in the process. The occurrence of nitrogen within the sample likely comes from the nitrogen in the plasma itself, effectively creating SnOxNy. The fabrication of SnOxNy thin films by ALD for battery anodes has been described by Steward et al.[36], which follows a similar process. As stated previously, they found that very long exposure times in the order of 20-100s were necessary to saturate the surface

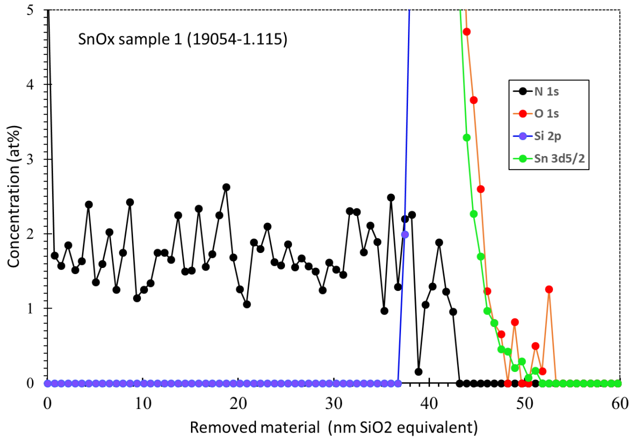

Figure 4.20: Elemental concentrations of plasma-assisted SnOx as determined by XPS, zoomed in to show the nitrogen concentration in the layer.

and remove methyl ligands. The assumption that the nitrogen plasma does not play a role due to the time-scale differences which are approximately 500 times shorter than found in literature, is false and the incorporation of nitrogen can be detected. Further research in this effect might be useful for research groups interested in the production of batteries by ALD.

XPS on plasma-assisted SnOx without water

Another interesting result is the XPS data for plasma-assisted SnOx without water, of which the results can be found in Figure 4.21. A high concentration of Sn is found, with values averaging 67% for the bulk. Interestingly both N and O are present, in roughly equal amounts. The amount of nitrogen decreases closer to the silicon wafer, but the amount of oxygen increases. This is due to the formation of a native SiO_2 layer on the Si substrates, which reflects in an increase in the amount oxygen in the same region. The growth in the first few cycles could possibly be influenced by this.

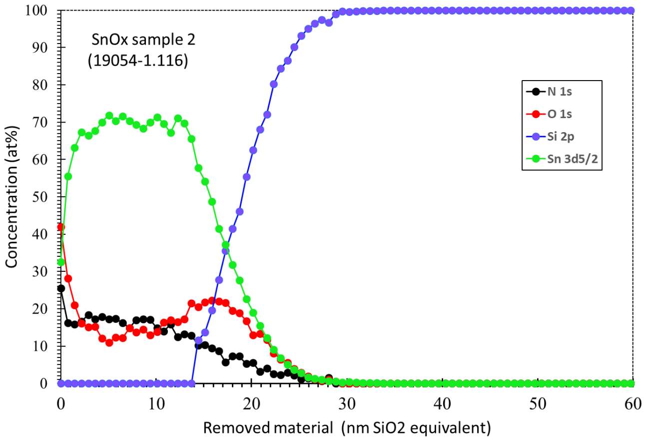

Figure 4.21: Elemental concentrations of a SnOx sample deposited without water.

As for the material composition, the material can best be described as either SnOxNy as described by Steward et al.[36] with some additional tin, or metallic Sn which has formed slight amounts of tin oxide and tin nitride. The silicon wafer starts at 14nm removed SiO_2 equivalent depth, compared to approximately 40 nm for the depositions. The SE model however gives it as seen in Figure 4.17 a comparable depth to the other materials of 60nm. This difference could be explained either due to the material being significantly easier to etch or the SE model not fitting properly to the material and giving the thin film layer a higher thickness than it has. Further research could look into measuring the thickness using different methods such as x-ray reflection to settle this matter.

XRD

To complement the XPS measurements and as a tool to learn more about the crystal structure of the material, grazing incidence XRD measurements are performed on all 4 sample types and the results are shown in Figure 4.22 together with selected peaks corresponding to Sn, SnO, SnO_2 or the silicon wafer.

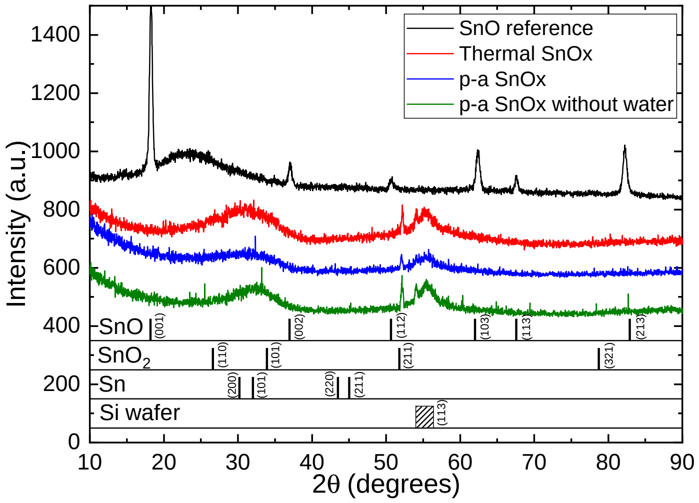

Figure 4.22: The grazing incidence XRD results for thermal SnOx, plasma-assisted SnOx, plasma-assisted SnOx without water and a reference SnO sample. Different peaks for bulk materials as found in the ICDD database are added as a reference. Due to the grazing incidence technique the (113) forbidden Si peak for the wafer is also detected.

The SnOx films obtained are in the nano-crystalline or amorphous state and only a few peaks can be seen. These results match with results found in literature[8,15,51] for amorphous SnOx. Most noticeably the broad peak around 30°, which for crystalline samples would be better defined as the (101) peak. The sharp peak around 55°is the result of using grazing incidence, as this corresponds to a forbidden (113) peak of the silicon wafer.

The spectra for thermal SnOx and plasma-assisted SnOx are very similar, and the lack of well-defined peaks except for a peak around 51°, which corresponds to SnO_2, makes it hard to draw conclusions about the material composition. In order to improve this, the samples will be annealed which will be discussed in section 4.3.5. The plasma-assisted SnOx without water sample shows an interesting spike at 83°which matches the (213) peak of the reference SnO. Due to its lack of width it can however not be concluded that it corresponds to tin monoxide.

Raman

Although a couple of peaks are visible on the XRD, the material still appears fully amorphous. To further confirm this, Raman spectroscopy is performed on the samples of which the results are shown in Figure 4.23. The spectra appear identical to the spectrum of an empty silicon wafer, conforming the amorphous nature by a lack of crystallinity in the sample. This could be due to the set-up not being sensitive enough to measure the thin film. The reference SnO sample for example shows excellent peaks in its XRD spectrum in Figure 4.22, but also appears identical to the wafer here where some deviation to the Si wafer in its Raman spectrum would have been expected. For further research thicker samples are therefore recommended.

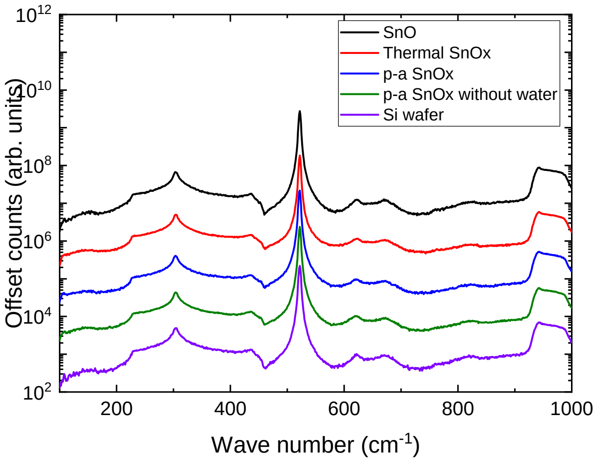

Figure 4.23: Raman spectroscopy on thermal SnOx, plasma-assisted SnOx, plasma-assisted SnOx without water and a reference SnO sample. A silicon wafer is added as a reference, and from there no significant differences can be seen.

4.3.4 Optical Properties

Optical analysis of the films was performed using UV-VIS spectroscopy. The transmission and reflectance of the various tin oxide and the reference tin monoxide are shown in Figure 4.24. The samples are approximately 100-120 nm in thickness, which is 1600 cycles compared to the 800 cycles for regular samples, deposited on a substrate of 0.5 mm of borosilicate glass. This change in substrate could influence the growth for the first couple of cycles, but this switch is a necessity as silicon wafers have poor optical transmission properties.

The transmission and reflectance can be found in Figure 4.24. The glass substrate shows a edge of transmittance above 3.5 eV and the reflectance increases at 4.6 eV. The thermal SnOx has peaks at different energies than the other samples, this could be due to an increased thickness compared to the other samples.

Compared to literature, the optical transmission of the plasma-assisted SnOx sample can be considered low, as tin oxide samples often reach 90%+ values under 3.0 eV[8]. The thermal SnOx sample does approach this value when compared to the glass sample. According to Toyama et al.[52], the drop in transmission can be explained by the presence of metallic Sn. This could be also the case here. Recalling the XPS data for the reference SnO sample, which has a composition of approximately 10% of metallic Sn and the reference SnO sample does show a low transmission in this Figure. Therefore, the lower can be seen as evidence for the reduction of Sn^{4+} by the hydrogen plasma. It should be noted that impurities from the present nitrogen could have a similar effect. For plasma-assisted SnOx this effect should be larger, which is indeed the case as the transmission is significantly lower.

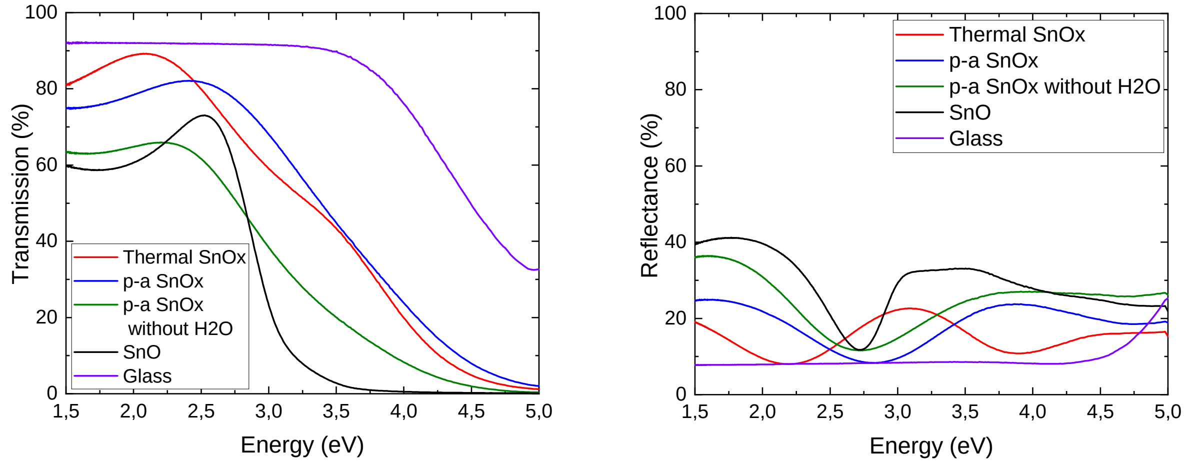

(a) **(b)**

Figure 4.24: Transmission (a) and reflectance (b) spectra for the various SnOx sample types. As a reference the values for glass and the reference tin monoxide sample are added.

The absorptance is calculated from the transmission and reflectance, which in turn can be used to determine the absorption coefficient α of the material using Equation 3.7 and 3.8. From here, the bandgap of the material can be deduced using Tauc plots. For this, the value $(\alpha \cdot E)^m$ is plotted against the energy, with m a power which is equal to $\frac{1}{2}$ for a material with an allowed indirect bandgap, and 2 for a direct bandgap.

The direct bandgap for (poly-) crystalline bulk SnO$_2$ as described in literature is 3.6-4.0 eV[53,54], which is in accordance to deposited SnO$_2$ thin films[26,55,25,56]. In comparison, SnO thin films have an indirect bandgap of 2.3-3.0 eV[15,57,20]. Therefore, the Tauc plots for both direct and indirect bandgaps are given in Figure 4.25.

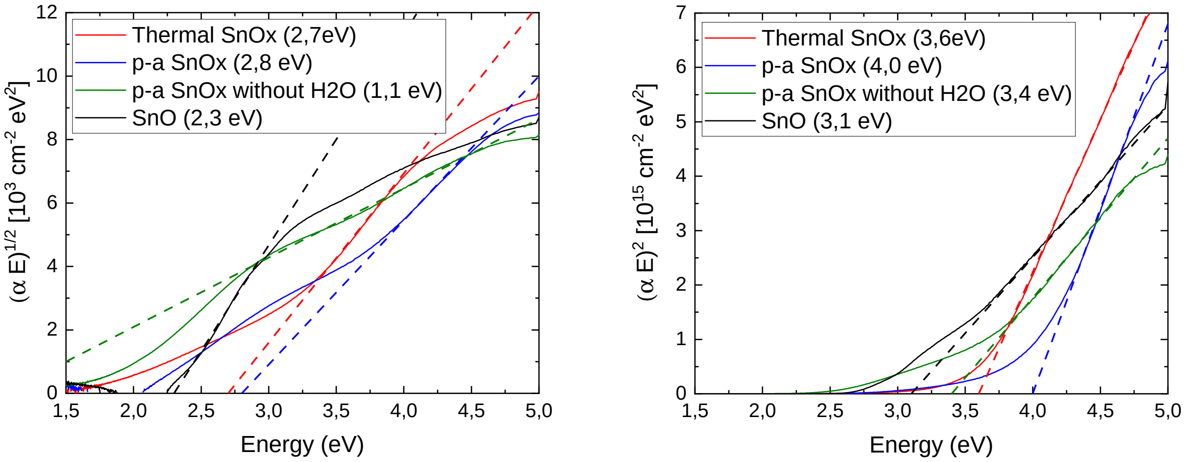

(a) **(b)**

Figure 4.25: Tauc plots for both indirect (a) and direct (b) bandgaps. Dotted lines are added at the linear parts to deduce the bandgaps.

The 2.3 eV indirect bandgap for SnO matches the findings of Lee et al.[57], but is on the lower end of other studies[15,20]. The bandgap values for the thermal and plasma-assisted SnOx are comparable to the literary values for tin dioxide mentioned above, which further indicates the material being tin dioxide instead of tin monoxide. The difference of 0.4 eV could be due to the incorporation of nitrogen and metallic tin as hypothesized before. The plasma-assisted SnOx without water with a direct bandgap of 3.4 eV approximates the tin monoxide.

4.3.5 Annealing

In the previous sections it was shown that the tin oxide samples are amorphous in nature. Although this result is not out of the ordinary, a polycrystalline thin film was preferred due to the superior electrical properties[6]. A way to change the crystallinity of the samples post-deposition is by annealing. The expected result is a slightly denser layer and the reduction of surface roughness. However, annealing a sample could also cause a chemical reaction to occur, changing the material composition. For example, it is possible to change the composition from tin monoxide to tin dioxide by annealing at 300 °C and above[58].

The annealing time and temperature to crystallize SnOx thin films vary a lot in literature. Some authors choose to be cautious and anneal barely above the deposition temperature with temperatures such as 180-200 °C[59,60], but the best results without changing the sample composition are achieved at 300 °C[51,55,61,30]. Therefore, the samples were annealed at 300 °C in air for 1 hour. Due to limited available equipment it was not possible to anneal the samples in a nitrogen or argon environment. The samples are measured with XRD before and after the annealing process, the results are found in Figure 4.26.

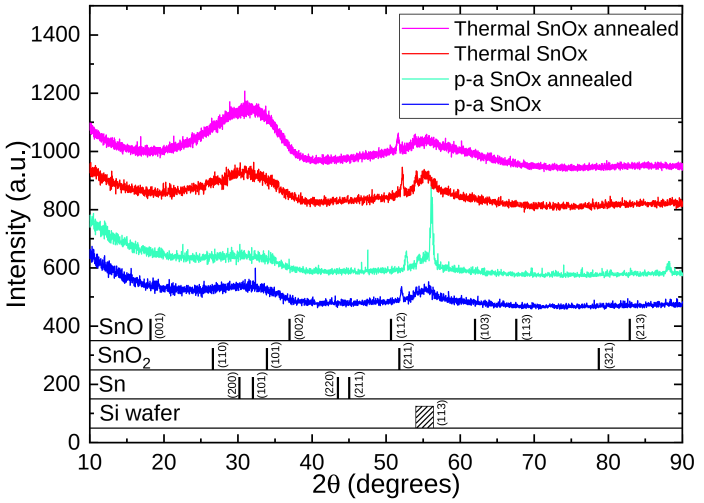

Figure 4.26: The grazing incidence XRD results for thermal and plasma-assisted SnOx before and after an anneal in air at 300 °C for 1 hour. Different peaks for bulk materials as found in the ICDD database are added as a reference. Due to the grazing incidence technique the (113) forbidden Si peak for the wafer is also detected.

The annealed thermal SnOx sample shows a more defined peak around 30°and a less defined peak for the silicon wafer. This could be a small increase in crystallinity, but the temperature of 300 °C for 1 hour is too low to make a significant difference. The plasma-assisted SnOx sample shows a large peak at 57°, which is attributed to the silicon wafer. However, for the forbidden [113] Si peak a broad peak is expected instead of such a well-defined peak. The only alternative explanation that could be found in literature is enhancement of the [002] SnO_2 peak at 57.9°, which normally is not visible, but is significantly enlarged for SnO_2 nanorods[62], which have a general preference to grow along the [001] direction. The growth of nanorods after annealing is considered to be incredibly unlikely by the author of this report, so this alternative explanation is considered to be speculationin need of further research.

The Raman spectra of the annealed samples are shown in Figure 4.27. From here it can be concluded that the samples after annealing are still fully amorphous and in-differentiable from the silicon wafer. These results do not match up with annealing in air results found in literature as mentioned above, so the annealing process should be re-evaluated. For further research the recommendation would be to increase the annealing temperature to for example 400°C.

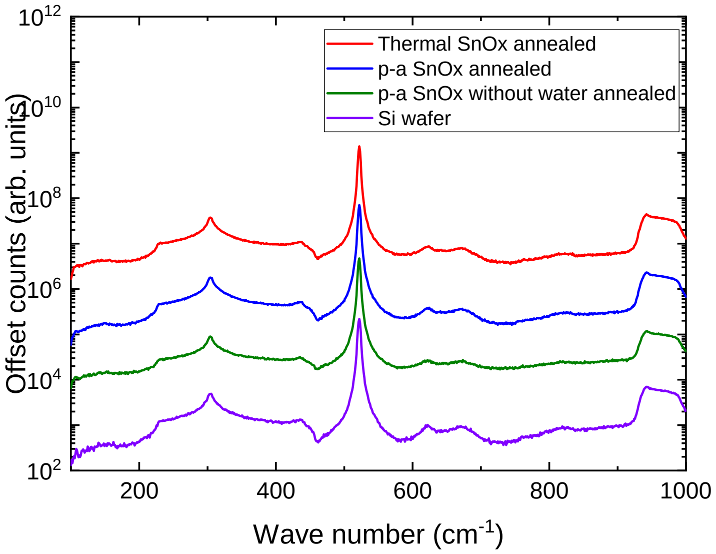

Figure 4.27: Raman spectroscopy on thermal SnOx, plasma-assisted SnOx and plasma-assisted SnOx without water after an anneal in air at 300 °C for 1 hour. A silicon wafer is added as a reference, and from there no significant differences can be seen.

Chapter 5

Conclusions and Final Remarks

The aim of this research was characterizing the plasma-assisted SnOx spatial atomic layer deposition process. The project started as a follow-up of research done at TNO/Holst Centre in which the possibilities of depositing p-type metal oxide thin films for the production of p-type thin film transistors were explored. This previous exploration concluded after literary research tin monoxide being the most likely candidate for this process. Problems arose early on in finding a suitable precursor, as TDMASn resulted in n-type tin dioxide. An innovative solution was proposed, by using an in-situ hydrogen plasma to reduce the oxidation state of tin from Sn^{4+} to Sn^{2+} or Sn^0 it might be possible to deposit tin monoxide instead.

This could not be confirmed however due to problems in the characterization, as differentiation between tin monoxide, dioxide or a mixture was found to be troublesome with the available equipment. This research continued by investigating the feasibility of using an hydrogen plasma as an additional step to the thermal SnOx process, showing the effect of various growth parameters, proposing reaction mechanisms and modelling the growth, and finally describing the difference in material properties from samples produced with the thermal and plasma-assisted SnOx process, and comparing those samples to tin monoxide reference samples.

5.1 Conclusions

Plasma-assisted SnOx depositions by SALD with TDMASn, H_2O and a H_2/N_2 plasma were performed and shown to be reproducible. The addition of an hydrogen plasma to the thermal deposition of SnOx resulted in a material with an increased refractive index of 2.1-2.2 compared to 1.9-2.0 for the process without plasma. As tin monoxide has a refractive index of 2.5-2.8, the deposited layers are considered to be closer to tin dioxide. The increase in refractive index is attributed to an increase in material density and the presence of a small amount of metallic tin.

This assumptions of both the thermal and plasma-assisted SnOx corresponding closer to tin dioxide is confirmed in XPS measurements, where the samples correspond closely to tin dioxide literary values and differ strongly from the reference tin monoxide sample. Measurements with XRD and UV-VIS also show the materials from both processes as similar, but significantly different from the reference tin monoxide.

The most significant difference in elemental concentration between thermal and plasma-assisted SnOx is the presence of 2% nitrogen in the plasma-assisted process. No carbon is detected with this nitrogen, so the nitrogen does not originate from the DMA ligands. The source of the nitrogen is the nitrogen plasma used in the process, which disproves the assumption made early on in this research of the nitrogen having such a low reactivity that it does not play a role in the process.

The hydrogen plasma does influence the material properties as seen with plasma composition variations. Increasing the amount of hydrogen in the plasma lowers the GPC and increases the refractive index for fractions up to 10% of the total 10 slm plasma flow, after which the values are saturated. Hall measurements for different hydrogen plasma ratios show similar results and an especially sharp decrease in the sheet resistance for even the slightest amount of hydrogen. This decrease in resistance is due to the incorporation of hydrogen doping within the thin film layer. For all SnOx processes Hall measurements show n-type materials.

The GPC versus the exposure time of the samples is thoroughly investigated for both thermal and plasma-assisted SnOx. Both processes show different saturation curves, which indicates different chemical reactions taking place. For thermal SnOx an overshoot is found for the rotation direction with a shorter purge time between the TDMASn and water, but not the other rotation direction. A model is shown which explains this effect due to additional water physisorption on the substrate which is not properly purged at certain exposure times.

The plasma-assisted SnOx saturation curves are shown to be solely dependant on the amount of precursor dosed to the substrate instead of the chemical reaction rate. Two different models with comparable performance are shown, a diffusion-limited mass transport model and a dosage-limited model utilizing the specific precursor dose of the system. The latter model was able to predict the effect of both of exposure time as well as precursor flow from the bubbler. Both models consider the chemical reaction to not be dependent on the number of hydroxyl ligands on the substrate surface. When deposition temperatures are varied, which directly influences the number of hydroxyl ligands on the substrate surface, the thermal SnOx shows a large variation in the GPC which is in accordance with literature. The plasma-assisted SnOx process however shows little to no temperature dependency.

The plasma-assisted SnOx process also shows no significant difference in the GPC and refractive index when water partial pressure is varied over two orders of magnitude. However, when no water at all is added to the sample there is no growth as expected for the thermal process, but the plasma-assisted process shows significant growth. The resulting material has a higher refractive index of 2.2-2.4 and is shown by XPS to consist of primarily tin with some oxygen and nitrogen, and most of the tin should be considered metallic.

Therefore, the hydrogen plasma does in-situ reduce the tin to a metallic state. However, by adding water as a co-reactant the tin is immediately re-oxidized. This results in a comparable layer to the tin dioxide from the thermal SnOx process, with some additional nitrogen and hydrogen and a slight amount of metallic tin present.

In conclusion, the addition of an hydrogen-nitrogen plasma to the thermal SnOx SALD process with TDMASn and water does not result in a p-type tin monoxide thin film. Although the plasma does reduce the tin in-situ and further research might yield insights in how to control the re-oxidation of tin, this method is as of yet not considered viable. Recommended would be the usage of a tin(II) precursor, it has been shown to result in a p-type metal oxide thin film layer.

5.2 Outlook

As in every project, some research could not be executed due to time constrains or set-up and/or budget limitations. This section will provide a starting point for follow-up research by highlighting some interesting leads found in this research that could not be pursued.

In the dosage-limited model the specific precursor dosage is shown to encompass the exposure time and precursor bubbler flow as a single parameter. It is however also dependent on the vapour pressure of the precursor. By varying the precursor temperature it could be investigated whether the results of varying vapour pressure could also be correctly predicted by this model.

Due to set-up limitations of the flow controllers it was not possible to test lower amounts of hydrogen in the plasma. Depositions have been performed with the lowest possible amounts, but the results between no hydrogen or just a little hydrogen are quite drastic when looking at the electrical properties, with a change in sheet resistance of four orders in magnitude. Finding the amount of hydrogen where this transition happens might yields some insight in the underlying mechanisms.

In all plasma-assisted deposition some nitrogen is present from the plasma. Using another non-reactive plasma like argon or helium would therefore likely result thin film layers with less impurities. This is especially interesting for the depositions without water, as the removal of nitrogen would possibly result in severely oxygen-deficient tin oxide thin films. Although this might be mostly hydrogen-doped metallic thin, careful oxidation could result in p-type tin monoxide films. If the amount of oxygen leaking into the reactor could be reduced the deposition of pure hydrogen-doped metallic tin might be possible.

Tin oxynitride as a material has some usage for the production of batteries. As mentioned multiple times throughout this report, the deposition of tin oxynitride layers by ALD has been shown by Steward et al.[36] and Ansari et al.[63]. However, to the best of the authors knowledge this might actually be the first time that possible SnOxNy thin films have been produced by SALD. However, it is still more likely to be a mixture of SnOx, SnNy and metallic tin. If interested in this material, this research can be used as a starting point. For the best results it is recommended to dose little to no water and to remove the hydrogen from the plasma mixture, as this would result in unwanted metallic tin and hydrogen doping.

Acknowledgements

The end is within reach, this project is almost done and I have to say, it wasn't an easy task. Many hours of work went into this project, and I couldn't have done it without the help from some amazing people.

First and foremost I would like to thank Corné, my main supervisor for this project. You brought me on this great adventure and many hours have we spend together in the lab and in meetings to tinker, discuss, brainstorm, make plans and what-not to solve the many problems which arose during this project. Thanks a lot for putting your trust in me and giving me all the freedom I could have ever wanted.

I've had a lot of help from the various members of the TNO/Holst ALD team. Everyone was always ready to answer any question that I had and willing to help with everything. A special shoutout to Willem, on whom I always could rely when something would not go as planned in the cleanroom.

My university supervisor, Erwin, has taught me a great deal in the past year. Although we did not meet that often, after every meeting I felt like I had gained some valuable insights on the project. Thanks a lot for supervising me! Also from the university, I would also like to thank Bart and Vincent for the collaboration on Hall measurements.

Special thanks to Willemijn, and with her all the students at Holst Centre. Dutch, Irish, French, Italian, Portuguese, it doesn't matter, you guys all grasped the concept of ”gezelligheid” and made it an awesome place to work!

Finally, a big kiss to my girlfriend Lisa. This year wasn't easy, and without your incredible support I wouldn't have made it. Sorry for the long nights, early meetings and having to put up with elevated stress levels. I'll make up to you!

Andy van der Velde
Eindhoven
December 2019

Appendix

A Spectroscopic Ellipsometry Models

In this section several SE models will be evaluated which can be used on standard 50-80nm SnOx samples used in this research. Other models than these mentioned are certainly possible, but would perform considerably worse.

Cauchy

The earliest dispersion formula was established by Cauchy in 1836 and is a simple empirical dispersion law. The ”Cauchy Transparent” dispersion can be defined as

$$n(\lambda) = A + \frac{B}{\lambda^2} + \frac{C}{\lambda^4} \tag{A.0.1}$$

with A a dimensionless parameter, which approximates the refractive index for $\lambda \to \infty$. B affects the curvature and amplitude for medium wavelengths in the visible range, while C affects the curvature and wavelength in the UV range.

Although Cauchy commonly used for its simplicity, the model cannot be easily applied to metals and semiconductors. The parameters do not have any physical meaning and the empirical relations are not Kramers-Kronig consistent as seen in Equation 3.6. This lack of predictive physical behaviour makes Cauchy, together with other empirical models such as Briot or Sellmeier, unfit for use in this research. It does provide a benchmark however to compare other SE models against.

New Amorphous Model

The new amorphous dispersion formula is a variant on the Forouhi-Bloomer amorphous dispersion model derived by Horiba Jobin Yvon[64]. It is applicable on amorphous semiconductors and dielectrics and takes into account the optical bandgap in the inter-band region It assumes localized atomic orbital overlap in which a band is formed, the valence and conduction band are parabolic shaped and are separated by a forbidden band with size E_g. As a model the accuracy is rather bad below the bandgap. The model predicts the complex refractive index, of which the extinction coefficient is given by

$$k(E) = \begin{cases} \frac{f_j \cdot (E-E_g)^2}{(E-E_j)^2+\Gamma_j^2} & \text{; for } E > E_g \\ 0 & \text{; for } E \leq E_g \end{cases}, \tag{A.0.2}$$

and the refractive index is

$$n(E) = n_\infty + \frac{B \cdot (E-E_j) + C}{(E-E_j)^2 + \Gamma_j^2} \text{ ,where } \begin{cases} B = \frac{f_j}{\Gamma_j} \cdot (\Gamma_j^2 - (E_j - E_g)^2) \\ C = 2 \cdot f_j \cdot \Gamma_j \cdot (E_j - E_g) \end{cases} \tag{A.0.3}$$

where f_j is a parameter between 0 and 1 which describes the strength of the extinction coefficient peak, Γ_j is the broadening term of the absorption peak, E_j is the energy at which the extinction is at a maximum and E_g is the bandgap energy.

Tauc - Lorentz

The most used model for SnOx is Tauc Lorentz. It wasdeveloped by Jellison and Modine in 1996 by combining the Tauc joint density of states and the Lorentx oscillator. It gives the complex dielectric function ε_{TL} as

$$\varepsilon_{TL} = \varepsilon_{r,TL} + i \cdot \varepsilon_{i,TL} = \varepsilon_{r,TL} + i \cdot (\varepsilon_{i,T} \times \varepsilon_{i,L}) \tag{A.0.4}$$

The imaginary part of the complex dielectric function $\varepsilon_{i,TL}$ is the product of the imaginary part of the Tauc dielectric function $\varepsilon_{i,T}$ and the Lorentz dielectric function $\varepsilon_{i,L}$. Approximating parabolic bands, inter-band transitions above the bandgap are given the Tauc dielectric function as

$$\varepsilon_{i,T}(E > E_g) = A_T \cdot (\frac{E - E_g}{E})^2 \tag{A.0.5}$$

with A_T the Tauc coefficient, E the photon energy and E_g the optical bandgap. For transitions below the bandgap, $\varepsilon_{i,T}(E \leq E_g) = 0$.

The imaginary part of the Lorentz oscillator is given by

$$\varepsilon_{i,L}(E) = \frac{A_L \cdot E_0 \cdot C \cdot E}{(E^2 - E_0^2)^2 + C^2 \cdot E^2} \tag{A.0.6}$$

in which A_L is the strength of the $\varepsilon_{i,TL}$ peak, C is the broadening term and E_0 the peak central energy. Multiplying these equations results in

$$\varepsilon_{i,TL}(E) = \varepsilon_{i,L} \times \varepsilon_{i,T} = \begin{cases} \frac{1}{E} \frac{AE_0C(E-E_g)^2}{(E^2-E_0^2)^2+C^2E^2} & ; \text{for } E > E_g \\ 0 & ; \text{for } E \leq E_g \end{cases} \tag{A.0.7}$$

where $A = A_T \times A_L$. The real part $\varepsilon_{r,TL}$ can be derived from this expression using the Kramers-Kronig relation in equation 3.6.

The requirement that $\varepsilon_{i,TL}$ should be zero for energies below the bandgap results in the model not taking intra-band absorption into account. Therefore, it might produce bad fits in that region.

Adachi - New Forouhi

An improvement of the new amourphous model mentioned earlier is the Adachi-New Forouhi model. The new amorphous model functions poorly at energies below the bandgap, which this model corrects by defining the dielectric constant ε as

$$\varepsilon(E) = \varepsilon_{Adachi}(E) + \varepsilon_{Forouhi}(E) \tag{A.0.8}$$

For which the first component $\varepsilon_{Adachi}(E)$, introduced by Ozaki and Adachi[65], describes the optical transitions from the valence band to the conduction band at 3D M_0 critical points, so from the valance band maximum to the conduction band minimum. ε_{Adachi} is defined as

$$\varepsilon_{Adachi}(E) = A_0 \cdot \left\{ \frac{f(\chi_0)}{E_g^{3/2}} + \frac{f(\chi_{S0})}{2 \cdot (E_g + \Delta_0)^{3/2}} \right\} \tag{A.0.9}$$

with A_0 a strength parameter, E_g the bandgap, Δ_0 the width of the energy split due to spin-orbit coupling, $f(\chi)$ a function to be applied to the susceptibilities χ_0 at E_g and χ_{SO} at $E_g + \Delta_0$

$$f(\chi) = \frac{2 - \sqrt{1+\chi} - \sqrt{1-\chi}}{\chi^2}, \chi_0 = \frac{E + i \cdot \Gamma_0}{E_g}, \chi_{S0} = \frac{E + i \cdot \Gamma_0}{E_g + \Delta_0} \tag{A.0.10}$$

in which Γ_0 is a broadening parameter.

The second part of equation A.0.8, $\varepsilon_1(E)$ is written as

$$\varepsilon_{Forouhi}(E) = (n_1(E) + i \cdot k_1(E))^2 \tag{A.0.11}$$

were $n(E)$ and $k(E)$ are from the new amorphous model as seen in equationsA.0.2 and A.0.3.

Further improvements can be made with an additional dielectric term from the Drude model ε_{Drude}[66] to take into account the contribution of free electrons in the conduction band. This would however add a couple of additional parameters which increases the amount of overfitting. The current SE set-up is unfortunately not capable of running these calculations.

Model Justification

An overview of the performance of the shown models is given in the Table below. Due to its excellent fits over the whole spectrum, the Adachi-New Forouhi model will be used as default for characterizing samples within this research. The New Amorphous and Tauc-Lorentz models are ill-suited for energies below the bandgap of the material, which is quite high (3.5-4.0 eV) in the case of SnOx. The Adachi-New Forouhi model is able to fit in this region.

It has to be said that this model gives a severe chance for overfitting. Therefore, whenever the Adachi - New Forouhi model produces unlikely results it will be compared to the Tauc-Lorentz model. For the majority of the cases, these models are in good accordance with each-other.

Table 5.1: An overview of the performance of different SE models on a reference plasma-assisted SnOx sample.

Model	Parameters	Range (eV)	χ^2	h (nm)	n(#)	k(#)	E_g(eV)
Cauchy	3	1,5-3,8	1,85	20,8±0,4	1,218	-0,602	3,313
		1,5-5,5	12,66	22,9±0,4	1,145	-0,481	3,971
New Amorphous	5	1,5-3,8	0,55	53,9±0,15	2,187	0,024	3,227
		1,5-5,5	1,83	54,8±0,17	2,147	0,032	3,188
Tauc-Lorentz	5	1,5-3,8	0,58	53,3±0,1	2,196	0,006	3,236
		1,5-5,5	1,23	52,5±0,1	2,171	0	3,233
Adachi-New Forouhi	8	1,5-3,8	0,049	50,0±0,09	2,273	-0,123	3,278
		1,5-5,5	0,37	55,2±0,09	2,204	0,031	3,190

Bibliography

[1] Xinge Yu, Tobin J Marks, and Antonio Facchetti. Metal oxides for optoelectronic applications. *Nature materials*, 15(4):383–396, 2016.

[2] Marius Grundmann, Heiko Frenzel, Alexander Lajn, Michael Lorenz, Friedrich Schein, and Holger von Wenckstern. Transparent semiconducting oxides: Materials and devices. *Physica status solidi (a)*, 207(6):1437–1449, 2010.

[3] Joon Seok Park, Wan-Joo Maeng, Hyun-Suk Kim, and Jin-Seong Park. Review of recent developments in amorphous oxide semiconductor thin-film transistor devices. *Thin solid films*, 520(6):1679–1693, 2012.

[4] Aprizal Sengrian. *p-Type Metal Oxide by Spatial Atomic Layer Depositon*. Internship report, University of Groningen, Holst Centre/TNO Eindhoven, March 2018.

[5] Luke Chadwick. *P-type Metal Oxide by Spatial Atomic Layer Deposition*. Internship report, Utrecht Universty, Holst Centre/TNO Eindhoven, November 2018.

[6] Zhenwei Wang, Pradipta K. Nayak, Jesus A. Caraveo-Frescas, and Husam N. Alshareef. Recent Developments in p-Type Oxide Semiconductor Materials and Devices. *Advanced Materials*, 28(20):3831–3892, 2016.

[7] MF Al-Kuhaili and MB Mekki. P-type conductivity in hydrogenated radio frequency sputtered tin oxide thin films. *Journal of Alloys and Compounds*, 772:801–807, 2019.

[8] C Guillén and J Herrero. P-type sno thin films prepared by reactive sputtering at high deposition rates. *Journal of Materials Science & Technology*, 35(8):1706–1711, 2019.

[9] BS Li, K Akimoto, and A Shen. Growth of cu2o thin films with high hole mobility by introducing a low-temperature buffer layer. *Journal of Crystal Growth*, 311(4):1102–1105, 2009.

[10] John E Crowell. Chemical methods of thin film deposition: Chemical vapor deposition, atomic layer deposition, and related technologies. *Journal of Vacuum Science & Technology A: Vacuum, Surfaces, and Films*, 21(5):S88–S95, 2003.

[11] Paul Poodt, David C Cameron, Eric Dickey, Steven M George, Vladimir Kuznetsov, Gregory N Parsons, Fred Roozeboom, Ganesh Sundaram, and Ad Vermeer. Spatial atomic layer deposition: A route towards further industrialization of atomic layer deposition. *Journal of Vacuum Science & Technology A: Vacuum, Surfaces, and Films*, 30(1):010802, 2012.

[12] P. Poodt, A. Illiberi, and F. Roozeboom. The kinetics of low-temperature spatial atomic layer deposition of aluminum oxide. *Thin Solid Films*, 532:22–25, 2013.

[13] David H Levy, Shelby F Nelson, and Diane Freeman. Oxide electronics by spatial atomic layer deposition. *Journal of Display Technology*, 5(12):484–494, 2009.

[14] X Du, Y Du, and SM George. In situ examination of tin oxide atomic layer deposition using quartz crystal microbalance and fourier transform infrared techniques. *Journal of Vacuum Science & Technology A: Vacuum, Surfaces, and Films*, 23(4):581–588, 2005.

[15] Hyo Yeon Kim, Ji Hyeun Nam, Sheby Mary George, Jin-Seong Park, Bo Keun Park, Gun Hwan Kim, Dong Ju Jeon, Taek-Mo Chung, and Jeong Hwan Han. Phase-controlled sno2 and sno growth by atomic layer deposition using bis (n-ethoxy-2, 2-dimethyl propanamido) tin precursor. *Ceramics International*, 45(4):5124–5132, 2019.

[16] Jonas Sundqvist, Aivar Tarre, Arnold Rosental, and Anders Hårsta. Atomic layer deposition of epitaxial and polycrystalline sno2 films from the sni4/o2 precursor combination. *Chemical Vapor Deposition*, 9(1):21–25, 2003.

[17] Jeong Hwan Han, Yoon Jang Chung, Bo Keun Park, Seong Keun Kim, Hyo-Suk Kim, Chang Gyoun Kim, and Taek-Mo Chung. Growth of p- Type Tin(II) Monoxide Thin Films by Atomic Layer Deposition from Bis(1-dimethylamino-2-methyl-2propoxy)tin and H 2 O. *Chemistry of Materials*, 26(Ii):6088–6091, 2014.

[18] Jere Tupala, Marianna Kemell, Miika Mattinen, Kristoffer Meinander, Sanni Seppälä, Timo Hatanpää, Jyrki Räisänen, Mikko Ritala, and Markku Leskelä. Atomic layer deposition of tin oxide thin films from bis[bis(trimethylsilyl)amino]tin(II) with ozone and water. *Journal of Vacuum Science & Technology A: Vacuum, Surfaces, and Films*, 35(4):041506, 2017.

[19] Jeffrey W Elam, David A Baker, Alexander J Hryn, Alex B F Martinson, Michael J Pellin, and Joseph T Hupp. Atomic layer deposition of tin oxide films using tetrakis(dimethylamino) tin. *Journal of Vacuum Science & Technology A: Vacuum, Surfaces, and Films*, 26(2):244–252, 2008.

[20] Seung-Hwan Lee, Jin-Myung Choi, Jae-Hong Lim, Jozeph Park, and Jin-Seong Park. A study on the thermoelectric properties of ald-grown aluminum-doped tin oxide with respect to nanostructure modulations. *Ceramics International*, 44(2):1978–1983, 2018.

[21] Marja N. Mullings, Carl Hägglund, and Stacey F. Bent. Tin oxide atomic layer deposition from tetrakis(dimethylamino)tin and water. *Journal of Vacuum Science & Technology A: Vacuum, Surfaces, and Films*, 31(6):061503, 2013.

[22] Lukas Hoffmann, Detlef Theirich, Daniel Schlamm, Tim Hasselmann, Sven Pack, Kai Oliver Brinkmann, Detlef Rogalla, Sven Peters, André Räupke, Hassan Gargouri, and Thomas Riedl. Atmospheric pressure plasma enhanced spatial atomic layer deposition of SnO x as conductive gas diffusion barrier. *Journal of Vacuum Science & Technology A: Vacuum, Surfaces, and Films*, 36(1):01A112, jan 2018.

[23] Dong-won Choi and Jin-Seong Park. Highly conductive sno2 thin films deposited by atomic layer deposition using tetrakis-dimethyl-amine-tin precursor and ozone reactant. *Surface and Coatings Technology*, 259:238–243, 2014.

[24] Bo-Eun Park, Jaehong Park, Sangyoon Lee, Sanghun Lee, Woo-Hee Kim, and Hyungjun Kim. Phase-controlled synthesis of snox thin films by atomic layer deposition and post-treatment. *Applied Surface Science*, 480:472–477, 2019.

[25] Yinghuan Kuang, Valerio Zardetto, Roderick van Gils, Saurabh Karwal, Dibyashree Koushik, Marcel A Verheijen, Lachlan E Black, Christ Weijtens, Sjoerd Veenstra, Ronn Andriessen, et al. Low-temperature plasma-assisted atomic-layer-deposited sno2 as an electron transport layer in planar perovskite solar cells. *ACS applied materials & interfaces*, 10(36):30367–30378, 2018.

[26] Lukas Hoffmann. *Spatial atomic layer deposition of electrically (non-) conductive gas diffusion barriers*. PhD thesis, Universität Wuppertal, Fakultät für Elektrotechnik, Informationstechnik und . . . , 2018.

[27] Jukka T Tanskanen and Stacey F Bent. Insights into the surface chemistry of tin oxide atomic layer deposition from quantum chemical calculations. *The Journal of Physical Chemistry C*, 117(37):19056–19062, 2013.

[28] H Schade, Z E Smith, JH Thomas III, and A Catalano. Hydrogen plasma interactions with tin oxide surfaces. *Thin Solid Films*, 117(2):149–155, 1984.

[29] KC Sabat, P Rajput, RK Paramguru, B Bhoi, and BK Mishra. Reduction of oxide minerals by hydrogen plasma: an overview. *Plasma Chemistry and Plasma Processing*, 34(1):1–23, 2014.

[30] P.-C. Hsu, C.-C. Wu, H. Hiramatsu, T. Kamiya, and H. Hosono. Film Texture, Hole Transport and Field-Effect Mobility in Polycrystalline SnO Thin Films on Glass. *ECS Journal of Solid State Science and Technology*, 3(9):Q3040–Q3044, 2014.

[31] Harm CM Knoops, Tahsin Faraz, Karsten Arts, and Wilhelmus MM Kessels. Status and prospects of plasma-assisted atomic layer deposition. *Journal of Vacuum Science & Technology A: Vacuum, Surfaces, and Films*, 37(3):030902, 2019.

[32] Y Creyghton, A van der Bruele, A Illiberi, F Roozeboom, and P Poodt. Atmospheric pressure plasma enhanced spatial atomic layer deposition. In *22nd International Symposium on Plasma Chemistry*, pages 1–4, 2015.

[33] Chris G Van de Walle. Hydrogen interactions with semiconductors and oxides. In *AIP Conference Proceedings*, volume 671, pages 33–39. AIP, 2003.

[34] J. B. Varley, A. Schleife, A. Janotti, and C. G. Van De Walle. Ambipolar doping in SnO. *Applied Physics Letters*, 103(8), 2013.

[35] E Langereis, HCM Knoops, AJM Mackus, F Roozeboom, MCM Van de Sanden, and WMM Kessels. Synthesis and in situ characterization of low-resistivity ta n x films by remote plasma atomic layer deposition. *Journal of Applied Physics*, 102(8):083517, 2007.

[36] David M Stewart, Alexander J Pearse, Nam S Kim, Elliot J Fuller, A Alec Talin, Keith Gregorczyk, Sang Bok Lee, and Gary W Rubloff. Tin oxynitride anodes by atomic layer deposition for solid-state batteries. *Chemistry of Materials*, 30(8):2526–2534, 2018.

[37] Philipp S Maydannik, Alexander Plyushch, Mika Sillanpää, and David C Cameron. Spatial atomic layer deposition: Performance of low temperature h2o and o3 oxidant chemistry for flexible electronics encapsulation. *Journal of Vacuum Science & Technology A: Vacuum, Surfaces, and Films*, 33(3):031603, 2015.

[38] Sebastian Franke, Matthias Baumkötter, Carsten Monka, Sebastian Raabe, Reinhard Caspary, Hans-Hermann Johannes, Wolfgang Kowalsky, Sebastian Beck, Annemarie Pucci, and Hassan Gargouri. Alumina films as gas barrier layers grown by spatial atomic layer deposition with trimethylaluminum and different oxygen sources. *Journal of Vacuum Science & Technology A: Vacuum, Surfaces, and Films*, 35(1):01B117, 2017.

[39] Raija Matero, Antti Rahtu, Mikko Ritala, Markku Leskelä, and Timo Sajavaara. Effect of water dose on the atomic layer deposition rate of oxide thin films. *Thin Solid Films*, 368(1):1–7, 2000.

[40] Kwang-Chon Kim, Beomjin Kwon, Hyun Jae Kim, Seung-Hyub Baek, Dow-Bin Hyun, Seong Keun Kim, and Jin-Sang Kim. Sn doping in thermoelectric bi2te3 films by metal-organic chemical vapor deposition. *Applied Surface Science*, 353:232–237, 2015.

[41] Eline Braeken. *Development and understanding of a plasma-assisted atomic layer deposition process for silicon nitride.* Master thesis, Eindhoven University of Technology, Eindhoven, August 2013.

[42] Sofyan A Taya, Taher M El-Agez, and Anas A Alkanoo. Ellipsometric configurations using a phase retarder and a rotating polarizer and analyzer at any speed ratio. *Chinese Physics B*, 21(11):110701, 2012.

[43] J Szuber, G Czempik, R Larciprete, D Koziej, and B Adamowicz. Xps study of the l-cvd deposited sno2 thin films exposed to oxygen and hydrogen. *Thin Solid Films*, 391(2):198–203, 2001.

[44] Riikka L Puurunen. Surface chemistry of atomic layer deposition: A case study for the trimethylaluminum/water process. *Journal of applied physics*, 97(12):9, 2005.

[45] Laurent Henn-Lecordier, Mariano Anderle, Erin Robertson, and Gary W Rubloff. Impact of parasitic reactions on wafer-scale uniformity in water-based and ozone-based atomic layer deposition. *Journal of Vacuum Science & Technology A: Vacuum, Surfaces, and Films*, 29(5):051509, 2011.

[46] DV Nazarov, NP Bobrysheva, OM Osmolovskaya, MG Osmolovsky, and VM Smirnov. Atomic layer deposition of tin dioxide nanofilms: a review. *Rev. Adv. Mater. Sci*, 40(3):262–275, 2015.

[47] Philipp S Maydannik, Tommi O Kaariainen, and David C Cameron. Continuous atomic layer deposition: Explanation for anomalous growth rate effects. *Journal of Vacuum Science & Technology A: Vacuum, Surfaces, and Films*, 30(1):01A122, 2012.

[48] JW Elam, D Routkevitch, PP Mardilovich, and SM George. Conformal coating on ultrahigh-aspect-ratio nanopores of anodic alumina by atomic layer deposition. *Chemistry of materials*, 15(18):3507–3517, 2003.

[49] Jaeyeong Heo, Adam S Hock, and Roy G Gordon. Low temperature atomic layer deposition of tin oxide. *Chemistry of Materials*, 22(17):4964–4973, 2010.

[50] Ling Yan Liang, Zhi Min Liu, Hong Tao Cao, Zheng Yu, Yuan Yuan Shi, Ai Hua Chen, Hai Zhong Zhang, Yan Qun Fang, and Xi Lian Sun. Phase and Optical Characterizations of Annealed SnO Thin Films and Their p-Type TFT Application. *Journal of The Electrochemical Society*, 157(6):H598, 2010.

[51] Ming-Hung Wu, Horng-Chih Lin, and Pei-Wen Li. Submicrometer p-type sno thin-film transistors fabricated by film profile engineering method. *IEEE Transactions on Electron Devices*, 66(4):1766–1771, 2019.

[52] Toshihiko Toyama, Yuichi Seo, Takafumi Konishi, Hiroaki Okamoto, Ryohei Morimoto, Yuichi Nishikawa, and Yasuo Tsutsumi. Optical absorption spectra of p-type tin monoxide thin films around their indirect fundamental gaps determined using photothermal deflection spectroscopy. *Thin Solid Films*, 555:148–152, 2014.

[53] J Melsheimer and D Ziegler. Band gap energy and urbach tail studies of amorphous, partially crystalline and polycrystalline tin dioxide. *Thin Solid Films*, 129(1-2):35–47, 1985.

[54] Matthias Batzill and Ulrike Diebold. The surface and materials science of tin oxide. *Progress in surface science*, 79(2-4):47–154, 2005.

[55] Saturi Baco, Abdullah Chik, and Fouziah Md Yassin. Study on optical properties of tin oxide thin film at different annealing temperature. *Journal of Science and Technology*, 4(1), 2012.

[56] B Selin Tosun, Rebekah K Feist, Aloysius Gunawan, K Andre Mkhoyan, Stephen A Campbell, and Eray S Aydil. Sputter deposition of semicrystalline tin dioxide films. *Thin Solid Films*, 520(7):2554–2561, 2012.

[57] Jung-Hoon Lee, Mi Yoo, DongHee Kang, Hyun-Mo Lee, Wan-ho Choi, Jung Woo Park, Yeonjin Yi, Hyun You Kim, and Jin-Seong Park. Selective sno x atomic layer deposition driven by oxygen reactants. *ACS applied materials & interfaces*, 10(39):33335–33342, 2018.

[58] H Giefers, F Porsch, and G Wortmann. Kinetics of the disproportionation of sno. *Solid state ionics*, 176(1-2):199–207, 2005.

[59] Jesus A. Caraveo-Frescas, Pradipta K. Nayak, Hala A. Al-Jawhari, Danilo B. Granato, Udo Schwingenschlögl, and Husam N. Alshareef. Record mobility in transparent p-type tin monoxide films and devices by phase engineering. *ACS Nano*, 7(6):5160–5167, 2013.

[60] H Luo, L Y Liang, Q Liu, and H T Cao. Magnetron-Sputtered SnO Thin Films for p-Type and Ambipolar TFT Applications. *ECS Journal of Solid State Science and Technology*, 3(9):Q3091–Q3094, 2014.

[61] B Alterkop, N Parkansky, S Goldsmith, and RL Boxman. Effect of air annealing on opto-electrical properties of amorphous tin oxide films. *Journal of Physics D: Applied Physics*, 36(5):552, 2003.

[62] Kan Zhao, Guofang Du, Li Luo, Guohui Qin, Qiuping Jiang, Yongju Liu, and Heyun Zhao. Novel multi-layered sno 2 nanoarray: self-sustained hydrothermal synthesis, structure, morphology dependence and growth mechanism. *CrystEngComm*, 17(9):2030–2040, 2015.

[63] Mohd Zahid Ansari, Dip K Nandi, Petr Janicek, Sajid Ali Ansari, Rahul Ramesh, Taehoon Cheon, Bonggeun Shong, and Soo-Hyun Kim. Low temperature atomic layer deposition of highly conformal tin nitride thin films for energy storage devices. *ACS applied materials & interfaces*, 2019.

[64] Horiba Jobin Yvon. New Amorphous Dispersion Formula. `https://www.horiba.com/fileadmin/uploads/Scientific/Downloads/OpticalSchool_CN/TN/ellipsometer/New_Amorphous_Dispersion_Formula.pdf`, 2006. Technical Note.

[65] Shunji Ozaki and Sadao Adachi. Spectroscopic ellipsometry and thermoreflectance of gaas. *Journal of applied physics*, 78(5):3380–3386, 1995.

[66] Michael Latzel, Manuela Göbelt, Gerald Brönstrup, Cornel Venzago, Sebastian W Schmitt, George Sarau, and Silke H Christiansen. Modeling the dielectric function of degenerately doped zno: Al thin films grown by ald using physical parameters. *Optical Materials Express*, 5(9):1979–1990, 2015.